



pubs.acs.org/cm Article

# Understanding the Amorphous Lithiation Pathway of the Type I Ba<sub>8</sub>Ge<sub>43</sub> Clathrate with Synchrotron X-ray Characterization

Andrew Dopilka, Amanda Childs, Svilen Bobey, and Candace K. Chan\*



Cite This: Chem. Mater. 2020, 32, 9444-9457



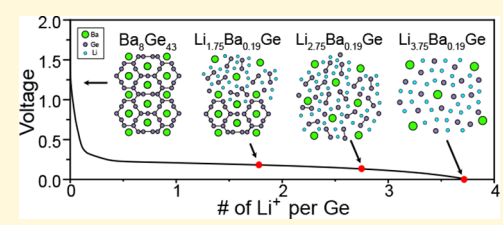
**ACCESS** I

III Metrics & More

Article Recommendations

Supporting Information

ABSTRACT: Tetrel (Tt = Si, Ge, and Sn) clathrates have highly tunable hostguest structures and have been investigated as novel electrode materials for Li-ion batteries. However, there is little understanding of how the clathrate structure affects the lithiation processes and phase evolution. Herein, the electrochemical lithiation pathway of type I clathrate Ba<sub>8</sub>Ge<sub>43</sub> is investigated with synchrotron Xray diffraction (XRD) and pair distribution function (PDF) analyses and compared to the lithiation of germanium with a diamond cubic structure ( $\alpha$ -Ge). The results confirm previous laboratory XRD studies showing that BagGe43 goes through a



solely amorphous phase transformation, which contrasts with the crystalline phase transformations that take place during lithiation of micrometer-sized  $\alpha$ -Ge particles. The local structure of framework-substituted clathrate Ba<sub>8</sub>Al<sub>16</sub>Ge<sub>30</sub> after lithiation is found to proceed through an amorphous phase transformation similar to that in BagGe43. In situ PDF and XRD during heating show that the amorphous phases derived from lithiation of Ba<sub>8</sub>Ge<sub>43</sub> are structurally related to various Li-Ge phases and crystallize at low temperatures (350-420 K). We conclude that the Ba atoms inside the clathrate structure act to break up the long-range ordering of Li-Ge clusters and kinetically prevent the nucleation and growth of bulk crystalline phases. The amorphous phase evolution of the clathrate structure during lithiation results in electrochemical properties distinct from those in  $\alpha$ -Ge, such as a single-phase reaction mechanism and lower voltage, suggesting possible advantages of clathrates over elemental phases for use as anodes in Li-ion

# 1. INTRODUCTION

Tetrel elements (Tt = Si, Ge, and Sn) are potential candidates for next-generation Li-ion battery anodes due to their intrinsically high capacities originating from a series of complex phase transformations. While the room-temperature lithiation of diamond-structured Si ( $\alpha$ -Si) proceeds through the formation of amorphous phases until crystallization of Li<sub>15</sub>Si<sub>4</sub> at high degrees of lithiation, 1,2 Ge and Sn readily crystallize at intermediate Li compositions to form various Li-Tt binary compounds.3-5 The phases that form have direct consequences on the electrochemical properties such as the voltage, rate capability, and stress evolution. Understanding how these properties are affected by the initial host structure and its subsequent lithiated intermediates is important for optimizing the performance of alloying anodes. Much work has been conducted on the role of nanostructuring on the alloying reactions of the elemental tetrels,  $^{6-11}$  but other than comparisons between amorphous and diamond-structured Si (or Ge) electrodes, 1,6,12-17 less focus has been given to understanding the effect of the initial crystal structure on the subsequent lithiation pathways.

To further this understanding, our group and others have been investigating tetrel clathrates and other polymorphs<sup>28-30</sup> for their electrochemical properties for Li-ion batteries. Tetrel clathrates are host-guest structures, wherein an open framework of covalently bound Tt atoms (all fourcoordinated and thus electroneutral) encapsulate metal guest atoms. For example, the type I clathrate adopts the Pm3n cubic space group with a general unit cell of M<sub>8</sub>Tt<sub>46</sub>, where M represents an alkali metal or alkaline earth metal guest atom. Clathrates can adopt several different crystalline structures and form with a variety of atomic substitutions and vacancies on guest or framework sites, resulting in a large design space for tuning the material properties of the clathrate. 31 The type I Ba-Ge clathrate, Ba<sub>8</sub>Ge<sub>43</sub>, deviates from the M<sub>8</sub>Tt<sub>46</sub> stoichiometry due to the presence of vacancies on Ge sites, which compensate for the excess electrons contributed from the Ba atoms. Substituting group III elements (Al, Ga, and In) for Ge allows for further charge compensation of Ba and results in the ability to tune the material properties of the clathrate. For instance, the electron precise Ba<sub>8</sub>Al<sub>16</sub>Ge<sub>30</sub> clathrate is a semiconductor,<sup>32</sup> while Ba<sub>8</sub>Ge<sub>43</sub> shows metallic-like behavior due to the excess electrons from Ba. 33 The structure of Ba<sub>8</sub>Ge<sub>43</sub> (Figure 1) is composed of two dodecahedra (Ge<sub>20</sub>) and six tetrakaidecahedra (Ge<sub>24</sub>) per formula unit, where all Ge atoms are in slightly distorted tetrahedral configurations. Much work

Received: September 12, 2020 Revised: September 21, 2020 Published: October 20, 2020





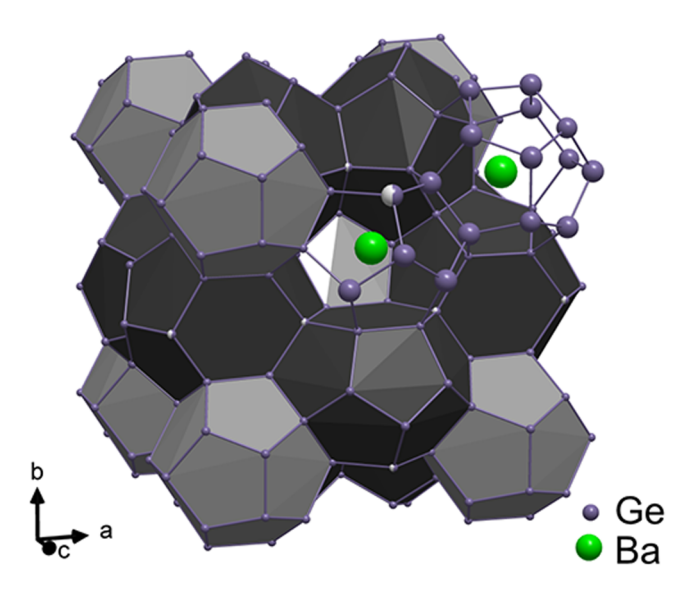


Figure 1. Crystal structure of type I  $Ba_8Ge_{43}$  clathrate (from ref 25). The purple spheres represent the Ge atoms, white spheres represent vacancies, and the green spheres represent the Ba atoms. The  $Ge_{20}$  and  $Ge_{24}$  polyhedra are shaded in gray and black, respectively.

has gone into understanding how the clathrate structure and defects affect the thermoelectric <sup>31,34,35</sup> and superconducting <sup>36–39</sup> properties of these materials; however, their role on the electrochemical and Li-ion alloying properties is less understood. Our goal in this work is to establish structure—property relationships for clathrates within the context of Li-ion battery applications.

Because of the similar covalent bonding within the cage-like framework in tetrel clathrates and their elemental analogues, the clathrates are expected to undergo similar alloying reactions with lithium. However, previous work shows that in some situations, this is not the case. For example, with laboratory X-ray diffraction analysis, we found previously that the type I  $Ba_8Al_yGe_{46-y}$  (0 < y < 16) clathrates proceed through an amorphous pathway different from the crystalline phase transformations typically seen in lithiation of  $\alpha$ -Ge. On the other hand, Si clathrates with a type II structure ( $Na_xSi_{136}$ ) 0 < x < 24) reacted with Li in a similar manner as  $\alpha$ -Si; however, if the Na occupancy of the cages was low, the voltage profile looked similar to that seen in the lithiation of amorphous Si. 18 From these studies, it appears that the guest atom type and occupancy in the clathrate are important parameters for determining their electrochemical properties. However, the formation of amorphous phases in the reaction intermediates precludes the use of Bragg diffraction for structural characterization, necessitating local structure characterization methods to understand the nature of the amorphous phases during the lithiation of clathrates.

Atomic X-ray pair distribution function (PDF) analysis has proven to be a vital tool in elucidating the alloying pathways of tetrel elements with alkali metals. 4.40-44 The PDF is derived from the total X-ray scattering pattern and provides information about the probability of finding atomic pairs at certain distances. This technique enables the local structure of amorphous and crystalline materials to be investigated, thus, allowing for a better picture of the lithiation intermediates to be attained. From this, differences in electrochemistry between clathrates and the elemental phases can be corroborated by differences in the structures formed during the lithiation

reactions. In addition, PDF analysis with *in situ* heating of electrochemically obtained amorphous phases can illuminate how the amorphous phases that form are related to known crystalline phases. For example, heating experiments on electrochemically synthesized amorphous Li<sub>x</sub>Si showed that the materials crystallized to Li–Si phases, implying that the local structure in the systems was similar. 46,47 Obtaining PDFs during this crystallization process could provide insights into how the amorphous structure relates to the crystalline structures.

In this work, the lithiation pathways of the type I clathrate Ba<sub>8</sub>Ge<sub>43</sub> are investigated in more detail with ex situ synchrotron X-ray PDF analysis and X-ray diffraction and compared to  $\alpha$ -Ge at similar states of lithiation. The PDF results confirm that Ba<sub>8</sub>Ge<sub>43</sub> proceeds through an amorphous pathway during lithiation, with no atomic correlations associated with longrange order observed beyond 10-30 Å. This contrasts with the crystalline phase transformations observed during lithiation of  $\alpha$ -Ge micrometer-sized particles, which are characterized by long-range order in both the XRD and PDF results. The local structure of the lithiated Ba<sub>8</sub>Al<sub>16</sub>Ge<sub>30</sub> clathrate, where Al is substituted on the Ge site, is found to be very similar to that seen in Ba<sub>8</sub>Ge<sub>43</sub> after electrochemical reaction with lithium. In situ heating during XRD and PDF measurements was conducted to evaluate the thermal stability of the amorphous phases and identify crystallization events and the phases that formed. Heating of the lithiated clathrate materials caused the amorphous Li-Ba-Ge phases to crystallize to Li-Ge binary compounds at low temperatures (350-420 K), suggesting structural relationships between the amorphous and crystalline phases. Our results show that analysis of the lithiation pathway of type I Ba<sub>8</sub>Ge<sub>43</sub> clathrate and comparison to the elemental analogue can provide an understanding of the effects of guest atoms and framework atoms on the lithiation pathways and their implications for Li-ion battery anodes.

## 2. EXPERIMENTAL METHODS

The Ba $_8$ Ge $_{43}$  and Ba $_8$ Al $_{16}$ Ge $_{30}$  clathrates were synthesized and prepared into electrodes in a similar manner as described in our previous work. The electrodes were lithiated galvanostatically in half-cells with lithium metal as counter electrode and then extracted for *ex situ* measurements. Synchrotron X-ray pair distribution (PDF) measurements were conducted at the Diamond Light Source (Didcot, United Kingdom) at the I15-I dedicated PDF beamline with  $\lambda$  = 0.161669 Å. The atomic PDF, G(r) as defined by Farrow and Billinge, was generated from the total scattering data using PDFgetX3 within the xPDFsuite software package. Synchrotron X-ray diffraction measurements were performed at the P02.1 powder diffraction beamline at PETRA III at the Deutsches Elektronen-Synchrotron (DESY) with  $\lambda$  = 0.20733 Å. More detailed descriptions of the synthesis, electrochemical and synchrotron measurements, and PDF analysis are in the Supporting Information.

### 3. RESULTS

**3.1.** Ex Situ XRD and PDF Analyses. To evaluate the local and long-range order of the lithiation intermediates, the Ba $_8$ Ge $_{43}$  and  $\alpha$ -Ge electrodes were electrochemically lithiated to different compositions and then subjected to ex situ synchrotron XRD and PDF measurements at room temperature. Scanning electron microscopy (SEM) of the electrodes showed that the Ba $_8$ Ge $_{43}$  sample was composed of irregularly shaped, micrometer-sized particles (2–10  $\mu$ m) with some larger shards (>20  $\mu$ m) and the  $\alpha$ -Ge sample was composed of similarly irregularly shaped, micrometer-sized particles (Figure

S1). Therefore, we assume that there are no nanosize effects on the structural or electrochemical observations made here. The voltage profiles and differential charge (dQ/dE) plots for the first lithiation of Ba<sub>8</sub>Ge<sub>43</sub> and  $\alpha$ -Ge are shown in Figure 2 with

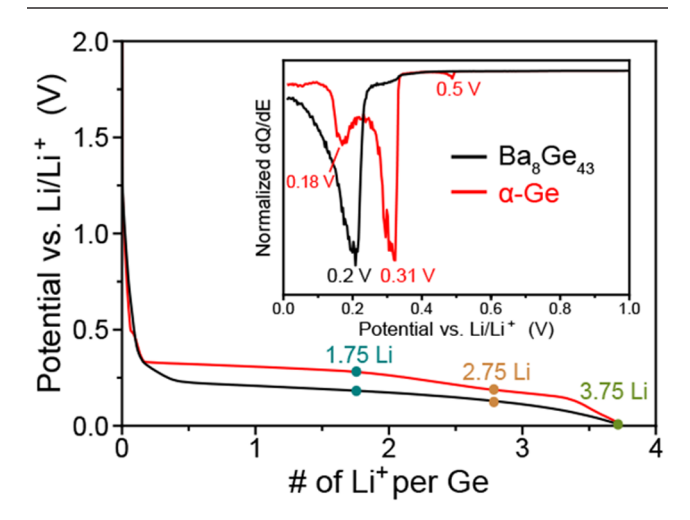


**Figure 2.** Voltage profile and corresponding dQ/dE plot of the lithiation of  $Ba_8Ge_{43}$  and  $\alpha$ -Ge at 25 mA/g (corresponding to C-rates of C/41 for  $Ba_8Ge_{43}$  and C/55 for  $\alpha$ -Ge) with a voltage cutoff of 10 mV vs Li/Li<sup>+</sup>. The blue, orange, and green circles represent the compositions at which cells were disassembled for *ex situ* PDF and XRD measurements.

blue, orange, and green points representing the compositions (as a ratio of Li to Ge) at which XRD and PDF samples were taken. The voltages and capacities of the cells at each of these points are presented in Table S1. The lithiation of Ba<sub>8</sub>Ge<sub>43</sub> is characterized by a plateau at 0.2 V versus Li/Li+ (seen as a large cathodic peak in the dQ/dE plot) and then a sloped decrease in voltage, consistent with our previous work. 25 In contrast, the voltage profile of  $\alpha$ -Ge has a higher reaction voltage starting around 0.3 V versus Li/Li<sup>+</sup>; the dQ/dE plot shows a small peak at 0.5 V from electrolyte reduction and two peaks corresponding to plateaus at 0.31 and 0.18 V, which represent a series of separate phase transformations.<sup>4</sup> The dQ/ dE plot of Ba<sub>8</sub>Ge<sub>43</sub> has a broad shoulder around 0.25-0.3 V, which is attributed to the presence of  $\alpha$ -Ge as impurity phase in the sample (shown later). Notably, both electrodes enable a reaction of 3.75 Li per Ge atom but the lower reaction voltage of Ba<sub>8</sub>Ge<sub>43</sub> suggests a difference in phase transformations during lithiation.

To understand the origin of the differences in these electrochemical features, the XRD and PDF patterns of  $\alpha$ -Ge and Ba<sub>8</sub>Ge<sub>43</sub> were compared at various degrees of lithiation at room temperature. The XRD and PDF results for the lithiation of  $\alpha$ -Ge are shown in Figure 3a,b, respectively, with reference patterns corresponding to Li<sub>5</sub>Ge<sub>2</sub><sup>51</sup> and Li<sub>15</sub>Ge<sub>4</sub>;<sup>52</sup> the results for the Ba<sub>8</sub>Ge<sub>43</sub> samples at similar Li compositions are shown in Figure 3c,d. Overall, the results for lithiation of  $\alpha$ -Ge are fairly consistent with those reported by Jung *et al.*,<sup>4</sup> although therein different voltage cutoffs were used to prepare the various samples rather than specific amounts of Li. (We acknowledge that there is substantial inconsistency in the literature <sup>3,8,53-55</sup> on the nature of the phases that form upon electrochemical lithiation of  $\alpha$ -Ge at room temperature, the results of which may be affected by the Ge particle size, current density used, and the characterization technique. For the sake

of consistency with the literature, we have chosen to only compare our results to those reported by Jung et al., wherein X-ray PDF was also used for analysis of micrometer-sized  $\alpha$ -Ge.) Following a reaction of 1.75 equiv of Li per Ge atom, a nominal composition referred to as Li<sub>1.75</sub>Ge hereafter, the XRD pattern shows reflections corresponding to  $\alpha$ -Ge and a lithium germanide phase we have tentatively identified as Li<sub>5</sub>Ge<sub>2</sub> with  $R\overline{3}m$  symmetry, indicating a two-phase reaction. This is supported by a Rietveld refinement analysis (Figure S2a and Table S2) fitting to the Li<sub>5</sub>Ge<sub>2</sub> and  $\alpha$ -Ge structures with phase fractions of 83 and 17%, respectively. In the work by Jung et al., Li<sub>7</sub>Ge<sub>3</sub> (reported as having P32<sub>1</sub>2 symmetry but this is likely an error as there is no such space group and it is likely intended to be P3212) was identified as a major intermediate phase during lithiation of  $\alpha$ -Ge and first-principles calculations suggested the energetic feasibility of this phase.<sup>51</sup> Li<sub>7</sub>Ge<sub>3</sub> and Li<sub>5</sub>Ge<sub>2</sub> have very similar structures where Ge-Ge dumbbells are arranged parallel to one another with slightly different amounts of Li surrounding them. As a result, the XRD and PDF patterns are nearly identical, making them difficult to differentiate. Our XRD results show that further lithiation of  $\alpha$ -Ge to an overall composition of Li<sub>2.75</sub>Ge resulted in the almost complete disappearance of the  $\alpha$ -Ge phase as well as a decrease and broadening of the reflections attributed to Li<sub>5</sub>Ge<sub>2</sub>. A reflection at  $2\theta = 5.4^{\circ}$  was also present in the diffraction pattern at this stage of the lithiation in the work by Jung et al.<sup>4</sup> and therein attributed to a disordered Li<sub>7</sub>Ge<sub>2</sub>-like phase. The XRD pattern of Li<sub>3.75</sub>Ge shows reflections corresponding to crystalline Li<sub>15</sub>Ge<sub>4</sub> and was fit well by Rietveld refinement analysis (Figure S2b and Table S3) with a lattice parameter of 10.7763(4) Å, consistent with previously reported results and the PDF pattern obtained here.

The details of the PDF refinements for the lithiation of the  $\alpha$ -Ge samples in Figure 3b are shown in Figure S3. The PDF of the pristine Ge particles could be refined with a good fit to the  $\alpha$ -Ge phase with  $R_{\rm w} = 8.2\%$  (Figure S3a). Lithiation to a composition of Li<sub>1.75</sub>Ge and a voltage of 0.28 V resulted in a PDF pattern containing  $\alpha$ -Ge correlations with a decreased intensity and the emergence of new correlations indicative of the presence of another phase. Refinement of the PDF was attempted using the structures of  $\alpha$ -Ge and several highly lithiated Li-Ge compounds commonly referred to as "dumbbell phases" (e.g., Li<sub>7</sub>Ge<sub>3</sub>, Li<sub>5</sub>Ge<sub>2</sub>, Li<sub>9</sub>Ge<sub>4</sub>, and Li<sub>7</sub>Ge<sub>2</sub>), <sup>51,56,57</sup> wherein parallel Ge-Ge dumbbells are surrounded by slabs of Li atoms. Calculated PDF patterns and crystal structures for these phases are presented in Figures S4 and S5, respectively. The best fit for the PDF from  $Li_{1.75}Ge$  ( $R_w = 19.1\%$ ) was obtained with 9.4 mol %  $\alpha$ -Ge and 90.6 mol % Li<sub>5</sub>Ge<sub>2</sub> (Figure S3b and Table S4). Fitting with Li<sub>7</sub>Ge<sub>3</sub> and Li<sub>9</sub>Ge<sub>4</sub> instead of  $\text{Li}_5\text{Ge}_2$  resulted in similar phase fractions and  $R_w$  values (19.7%) for Li<sub>7</sub>Ge<sub>3</sub> and 22.9% for Li<sub>9</sub>Ge<sub>4</sub>), which is consistent with the nearly identical arrangement of Ge-Ge dumbbells in these phases (see Figure S5a-c). At a composition of Li<sub>2.75</sub>Ge and a voltage of 0.17 V, the best fit attained was from a combination of Li<sub>13</sub>Ge<sub>5</sub> (64.3%) and Li<sub>7</sub>Ge<sub>2</sub> (35.7%) (Figure S3c and Table S5), similar to the results reported by Jung et al., 4 wherein multiple combinations of Ge-Ge dumbbell phases resulted in comparable fits. We found that fitting to Li<sub>7</sub>Ge<sub>3</sub> and Li<sub>5</sub>Ge<sub>2</sub> also resulted in decent fits (Table S5), which suggests that the Ge-Ge dumbbells are the dominant local features present in the electrode at this point in the lithiation process. The fact that the PDF for Li<sub>2.75</sub>Ge can be fit comparably to multiple phases, as well as the broadness of the reflections in the XRD

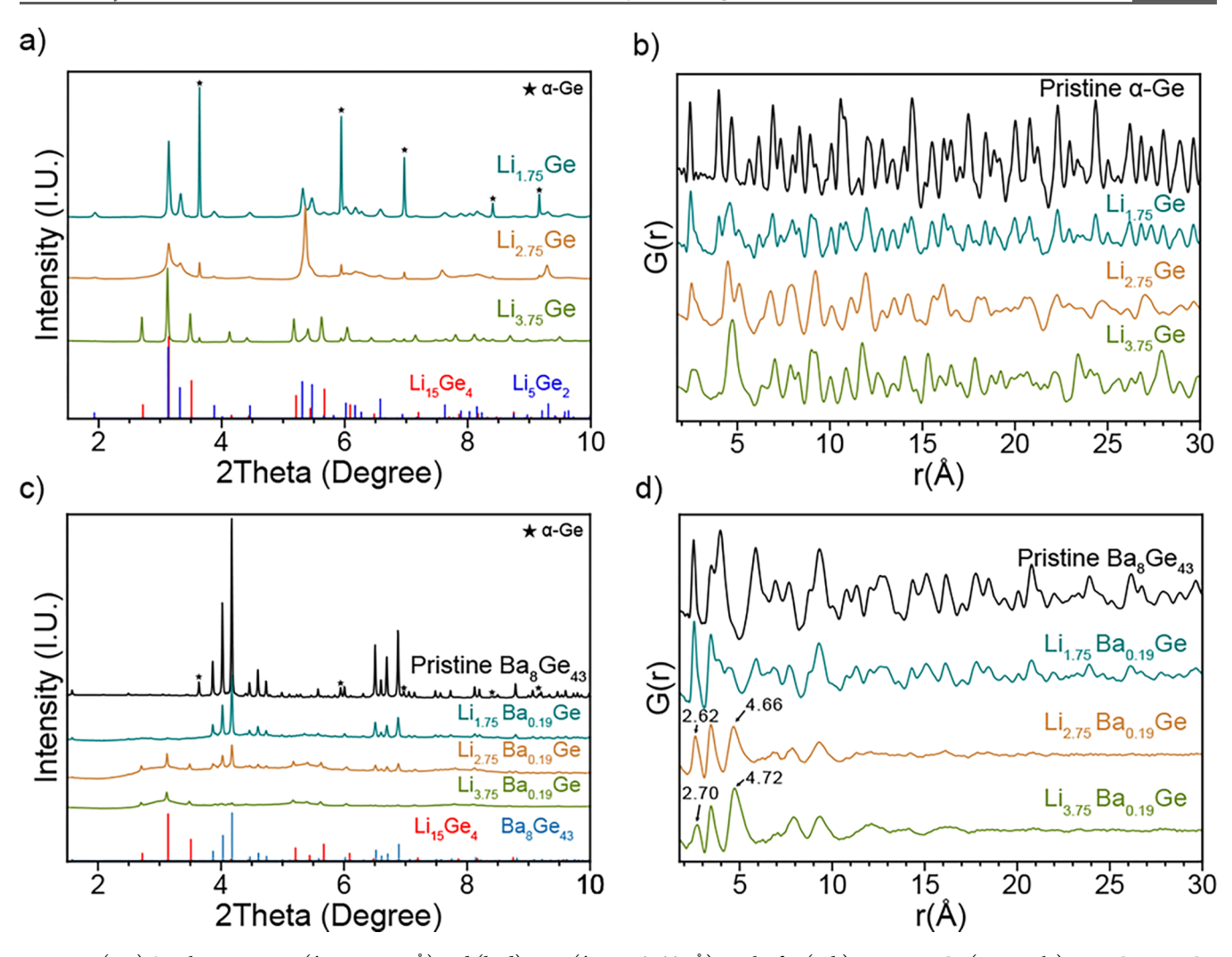


Figure 3. (a, c) Synchrotron XRD ( $\lambda$  = 0.20733 Å) and (b, d) PDF ( $\lambda$  = 0.161669 Å) results for (a, b) pristine α-Ge (PDF only), Li<sub>1.75</sub>Ge, Li<sub>2.75</sub>Ge, and Li<sub>3.75</sub>Ge and (c, d) pristine Ba<sub>8</sub>Ge<sub>43</sub>, Li<sub>1.75</sub>Ba<sub>0.19</sub>Ge, Li<sub>2.75</sub>Ba<sub>0.19</sub>Ge, and Li<sub>3.75</sub>Ba<sub>0.19</sub>Ge.

pattern, suggests that the structure is disordered but maintains a local structural motif of Ge-Ge dumbbells and isolated Ge atoms. At a composition of Li<sub>3.75</sub>Ge, the PDF could be fit to  $Li_{15}Ge_4$  with  $R_w = 22.9\%$  (Table S6), the structure of which consists of isolated Ge atoms surrounded by Li. The addition of a Li-Ge dumbbell phase resulted in a better fit  $(R_w =$ 11.8%) with 85.7 mol %  $Li_{15}Ge_4$  and 14.3 mol %  $Li_7Ge_3$ (Figure S3d and Table S6). The modest improvement in the fitting suggests that the Li-Ge dumbbell phases, the primary structrual motifs identified prior to this point, have been mostly consumed by the addition of more Li atoms and breaking of the Ge-Ge bonds in the structure. The observation of a dumbbell phase in the PDF of the fully lithiated Ge is consistent with the results from Jung et al., wherein it was suggested that Li<sub>15</sub>Ge<sub>4</sub> could decompose after formation. Alternatively, there still could be residual Ge-Ge bonding in the material. A similar observation was made after lithiation of  $\alpha$ -Si, <sup>40</sup> where Li<sub>15</sub>Si<sub>4</sub> was found to have crystallized after full lithiation but features from Si-Si dumbbells were still observed in the PDF.

The synchrotron XRD patterns of the  $Ba_8Ge_{43}$  samples are shown in Figure 3c with reference patterns for  $Li_{15}Ge_4$  and  $Ba_8Ge_{43}$ . The XRD pattern for the as-synthesized  $Ba_8Ge_{43}$  clathrate shows a small amount of  $\alpha$ -Ge as the secondary

phase, possibly resulting from Ba loss via evaporation during the clathrate synthesis. After addition of 1.75 Li per Ge atom (i.e., to a composition of Li<sub>1.75</sub>Ba<sub>0.19</sub>Ge and a voltage of 0.175 V versus Li/Li<sup>+</sup>), the reflections corresponding to the Ba<sub>8</sub>Ge<sub>43</sub> phase decrease in intensity without any new reflections appearing, confirming that the Ba<sub>8</sub>Ge<sub>43</sub> converts to an amorphous phase upon lithium insertion, consistent with our previous observations by laboratory XRD.<sup>25</sup> Subsequent lithiation to a composition of Li<sub>2.75</sub>Ba<sub>0.19</sub>Ge results in a further decrease in the Ba<sub>8</sub>Ge<sub>43</sub> reflections and the appearance of reflections corresponding to Li<sub>15</sub>Ge<sub>4</sub>. At this point in the reaction, the cell has reached a voltage of 0.11 V versus Li/Li<sup>+</sup> (Table S1), which is below the potential where  $\alpha$ -Ge can be converted to Li<sub>15</sub>Ge<sub>4</sub>.<sup>4</sup> Therefore, we attribute the origin of  $Li_{15}Ge_4$  to the reaction of Li with the  $\alpha$ -Ge impurity phase, not the clathrate phase. Upon further lithiation to Li<sub>3.75</sub>Ba<sub>0.19</sub>Ge, the XRD pattern only shows reflections attributed to Li<sub>15</sub>Ge<sub>4</sub> formed from the impurity phase reaction, confirming that the lithiated clathrate phase is amorphous.

The corresponding PDF patterns for Ba<sub>8</sub>Ge<sub>43</sub> at different degrees of lithiation are shown in Figure 3d. The X-ray PDF measurement is sensitive to the atomic scale correlations between pairs of atoms, giving insight into the local structuring of Ge, Li, and Ba atoms. The intensity of the correlations is

dependent on the atomic number and concentration of the elements, meaning that Ge correlations (Ge–Ge, Ge–Li, and Ge–Ba) are expected to contribute the most to the observed patterns in the clathrate. Refinement of the PDF for the pristine clathrate showed that there was a minimal amount (4.4 mol %) of  $\alpha$ -Ge as a secondary phase (Figure S6a and Table S7), confirming the XRD results. In the low r region, the PDF shows correlations at ca. 2.51, 3.50, 3.96, and 5.92 Å (Figure 3d). Inspection of the simulated partial PDFs (Figure S4a) shows that these correlations correspond to direct Ge–Ge bonding, Ba–Ge correlations, next nearest neighbor Ge–Ge distances, and third nearest neighbor Ge–Ge distances, with minimal contributions from Ba–Ba correlations due to the large separation distance of the Ba atoms ( $\sim$ 6 Å) in the clathrate structure (Figure S4a).

By observing how these correlations change with increasing amounts of lithium addition to Ba<sub>8</sub>Ge<sub>43</sub>, the average local structure of the lithiated intermediate phases can be determined. After addition of 1.75 Li per Ge, the PDF shows that the correlations decrease in the intensity relative to the pristine sample. Significant changes are seen at low r values, while the pattern at high r values (10–30 Å) resembles that for the pristine clathrate. Refinement of the pattern to the Ba<sub>8</sub>Ge<sub>43</sub> structure from 10 < r < 30 Å confirms that the high r correlations match reasonably well with those for the pristine clathrate (Figure S6b and Table S7). The difference curve of the refinement from 2 < r < 30 Å reveals correlations at 2.62, 3.42, and 4.50 Å (Figure S6c) but no other features at r > 10 Å, suggesting that these low r correlations arise from an amorphous, lithium-containing phase that coexists with the pristine clathrate.

Upon addition of lithium to reach the composition of Li<sub>2.75</sub>Ba<sub>0.19</sub>Ge (at 0.11 V vs Li/Li<sup>+</sup>), it is apparent that the Ba<sub>8</sub>Ge<sub>43</sub> starting material has been completely reacted and the PDF lacks noticeable features at r > 10 Å, indicating the absence of long-range order. The PDF for Li<sub>2.75</sub>Ba<sub>0.19</sub>Ge (Figure 3d) shows features very similar to those in the difference plot obtained in the refinement for Li<sub>1.75</sub>Ba<sub>0.19</sub>Ge to the Ba<sub>8</sub>Ge<sub>43</sub> structure (Figure S6d). The first peak at 2.62 Å is similar in position to that found in Li-Ge dumbbell phases, wherein the Ge-Ge (~2.4 to 2.6 Å) and Li-Ge correlations ( $\sim$ 2.7 to 2.8 Å) contribute to the first peak in the PDF (Figure S4). The second peak at 3.44 Å is typical of Ba-Ge distances (e.g., such as that in BaGe<sub>2</sub>)<sup>58</sup> but slightly shorter than the 3.5– 3.9 Å lengths for these Ba-Ge distances in the pristine clathrate phase (Figure S4a). The third peak at 4.66 Å is similar to the distance separating Ge dumbbells from each other (4.4–5.2 Å) in Li–Ge dumbbell phases.

Further lithiation to a composition of Li<sub>3.75</sub>Ba<sub>0.19</sub>Ge (a voltage of 10 mV) results in a PDF that is very similar to the one seen for Li<sub>2.75</sub>Ba<sub>0.19</sub>Ge but with slightly shifted correlations and intensities (Figure 3d). The peak at 2.62 Å for Li<sub>2.75</sub>Ba<sub>0.19</sub>Ge related to Ge–Ge and Li–Ge bonds is less intense and is shifted to 2.70 Å in Li<sub>3.75</sub>Ba<sub>0.19</sub>Ge, suggesting that fewer direct Ge–Ge bonds are present. The peak at 4.66 Å is shifted to 4.72 Å and is more intense relative to the peak at 2.70 Å, suggesting an increase in correlations arising from separated Ge atoms relative to the correlations from the Ge–Ge bond in the dumbbells. As the Li content increases relative to Ge, it is expected that more isolated Ge atoms surrounded by Li will be present compared to Ge dumbbells, as seen in the Li<sub>15</sub>Ge<sub>4</sub> (Li<sub>3.75</sub>Ge) phase where no dumbbells are present (Figure S5e). Overall, the PDFs of the Ba<sub>8</sub>Ge<sub>43</sub> samples after

the reaction with lithium suggest that the lithiation proceeds through a two-phase conversion of the pristine, crystalline clathrate into an amorphous phase, corroborating the presence of a constant voltage plateau in the voltage profile. The amorphous phases have similar local structures as those found in Li—Ge phases, with the addition of a correlation at 3.44 Å from Ba—Ge bonds.

PDF analysis of the Ba<sub>8</sub>Ge<sub>43</sub> sample after one full lithiation/ delithiation cycle was also performed and is shown in Figure S7 along with the corresponding voltage profile and dQ/dEplot (Figure S7a,b). The lithiation/delithiation voltage profile of  $\alpha$ -Ge is provided as well to demonstrate that the delithiation pathway is different for  $Ba_8Ge_{43}$ . In  $\alpha$ -Ge, there are two plateaus during delithiation (at 0.41 and 0.62 V vs Li/Li<sup>+</sup>) consistent with a previous report,<sup>41</sup> while the delithiation of  $Ba_8Ge_{43}$  showed a broad peak in the dQ/dE plot at 0.3 V with a gradually sloped voltage profile. The PDF of Ba<sub>8</sub>Ge<sub>43</sub> after full lithiation and delithiation showed no long-range correlations at r > 10 Å, indicating that the delithiated Ba<sub>8</sub>Ge<sub>43</sub> is amorphous (Figure S7c). There is a correlation centered at 2.52 Å corresponding to Ge-Ge bonding and a broad peak at 3.43 Å from Ba-Ge correlations with a broad shoulder at ~3.96 Å, which is close to the next nearest neighbor Ge distance in Ba<sub>8</sub>Ge<sub>43</sub>. The PDF for the pristine, crystalline Ba<sub>8</sub>Ge<sub>43</sub> and the amorphous Ba<sub>8</sub>Ge<sub>43</sub> after delithiation (Figure S7d) show features with similar peak positions, implying that they have very similar local structures. This suggests that although the clathrate structure undergoes an amorphous phase transformation after addition of lithium, the local structure of the subsequent amorphous phase after lithium is removed resembles that seen in the original crystalline structure. In other words, despite the crystallineto-amorphous transition, the local structural features of the clathrate are retained after one cycle.

The Al-substituted clathrate, Ba<sub>8</sub>Al<sub>16</sub>Ge<sub>30</sub>, was also subjected to PDF analysis after full lithiation to an amount of 1.9 Li per (Al + Ge) atom. The voltage profile and corresponding dQ/dEplot are presented in Figure S8 along with the PDF refinement (Table S8) of the pristine Ba<sub>8</sub>Al<sub>16</sub>Ge<sub>30</sub> and PDF after the reaction with 1.9 Li to a total composition of Li<sub>1.9</sub>Ba<sub>0.17</sub>Al<sub>0.35</sub>Ge<sub>0.65</sub>. Consistent with our previous work, <sup>25</sup> the Al-substituted clathrate reacted at a lower voltage of 0.06 V versus Li/Li<sup>+</sup> compared to 0.2 V of Ba<sub>8</sub>Ge<sub>43</sub> but displayed a lower capacity than that for Ba<sub>8</sub>Ge<sub>43</sub>. The PDF plot for the most lithiated composition (Figure S8c) showed that a significant amount of crystalline fraction was present, which could be fit well to the pristine Ba<sub>8</sub>Al<sub>16</sub>Ge<sub>30</sub> structure, meaning that the original clathrate phase was not fully reacted. Similar to the refinement for Li<sub>1.75</sub>Ba<sub>0.19</sub>Ge (Figure S6c), the difference pattern of the refinement for  $Li_{1.9}Ba_{0.17}Al_{0.35}Ge_{0.65}$  revealed an amorphous phase with correlations at 2.64, 3.45, and 4.57 Å, suggesting the formation of a similar amorphous phase as that seen in the lithiation of Ba<sub>8</sub>Ge<sub>43</sub>. This suggests that the lithiation of Ba<sub>8</sub>Al<sub>16</sub>Ge<sub>30</sub> proceeds in a similar manner to Ba<sub>8</sub>Ge<sub>43</sub>; however, the presence of Al in the amorphous phase results in a lower reaction voltage and capacity compared to

**3.2.** *In Situ* **Heating PDF Studies.** As described in the previous section, visual comparison of the PDFs for  $Ba_8Ge_{43}$  and  $\alpha$ -Ge after lithiation shows similarities in peak positions at low r values (2–5 Å), suggesting similar local structures for the Li and Ge atoms. However, the assignment of the broad peaks from 6 to 10 Å in the lithiated clathrate samples is less obvious

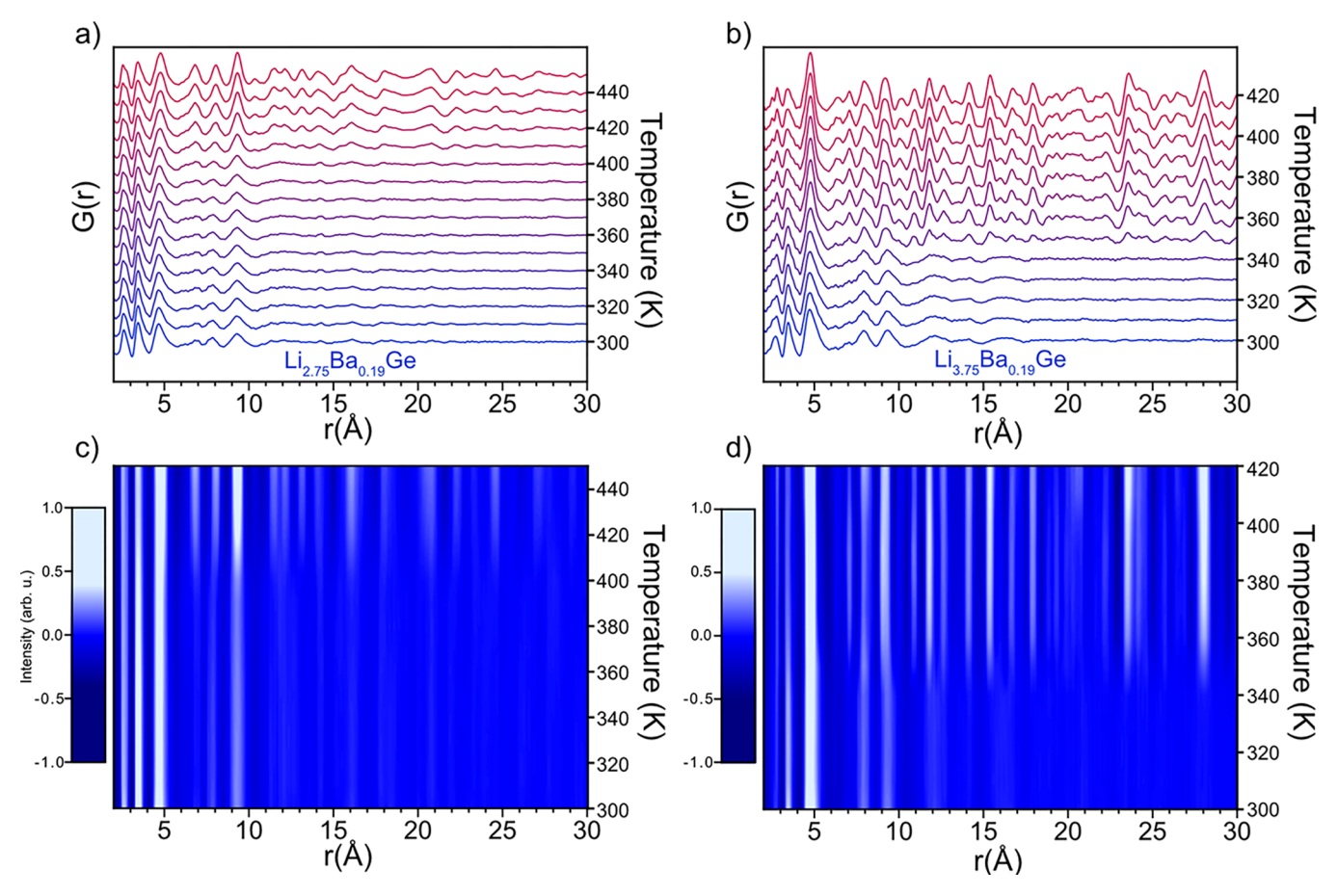


Figure 4. (a) In situ PDF measurements during heating of the lithiated Ba<sub>8</sub>Ge<sub>43</sub> (Li<sub>2.75</sub>Ba<sub>0.19</sub>Ge) from 300 to 450 K. (b) In situ PDF measurements during heating of the fully lithiated Ba<sub>8</sub>Ge<sub>43</sub> (Li<sub>3.75</sub>Ba<sub>0.19</sub>Ge) from 300 to 420 K. PDF scans were taken for 10 min intervals with the temperature held at every 10 K; patterns are *y*-offset for clarity. (c, d) Corresponding false colormaps for Li<sub>2.75</sub>Ba<sub>0.19</sub>Ge and Li<sub>3.75</sub>Ba<sub>0.19</sub>Ge, respectively; a linear interpolation was used between measured data points.

and could originate from Ge-Ge, Ba-Ge, and Li-Ge correlations. To identify the origin of these correlations, variable-temperature PDF measurements were conducted to evaluate the lithiated Ba<sub>8</sub>Ge<sub>43</sub> structures upon moderate heating and their relationship to the original amorphous structure. Figure 4a,b shows PDFs of Ba<sub>8</sub>Ge<sub>43</sub> lithiated to compositions of Li<sub>2.75</sub>Ba<sub>0.19</sub>Ge and Li<sub>3.75</sub>Ba<sub>0.19</sub>Ge acquired during in situ heating from room temperature to 450 and 420 K, respectively. The corresponding false colormaps are shown underneath in Figure 4c,d, where the light blue and dark blue shadings indicate regions of higher and lower intensities, respectively. For Li<sub>2.75</sub>Ba<sub>0.19</sub>Ge (Figure 4a,c), there is little change in the PDF pattern until reaching a temperature of 410 K, where the broad peaks from 6 to 10 Å begin to sharpen and noticeable long-range correlations begin to appear out to 30 Å, indicating that crystallization is occurring. After heating to 450 K, the peaks sharpen further, suggesting a higher degree of ordering. In the case of Li<sub>3.75</sub>Ba<sub>0.19</sub>Ge (Figure 4b,d), crystallization occurred at a lower temperature of 350 K, as seen by the appearance of correlations at r > 10 Å. As in Li<sub>2.75</sub>Ba<sub>0.19</sub>Ge, the broad peaks originally around 2–10 Å begin to sharpen as the crystallization occurred.

To better illustrate the structural features, the PDFs of the lithiated clathrate samples before and after heating are shown in Figure 5, along with the PDF of the  $\alpha$ -Ge sample lithiated to the same composition for comparison. Visual inspection shows that the PDFs contain similar features, indicating that the heat-

induced crystallization process produced a structure in the lithiated clathrate that was similar to that found in the Li–Ge phases that evolved from lithiation of  $\alpha$ -Ge at room temperature. This is supported by comparison of structure functions of the same sets of samples, wherein Bragg peaks in comparable positions are present, suggesting similarities in the crystalline phases in each sample (Figure S9).

For the Li<sub>2.75</sub>Ba<sub>0.19</sub>Ge PDFs (Figure 5a), three correlations are present from 2 to 5 Å while two sets are present in the Li<sub>2.75</sub>Ge PDF. The correlation centered at 3.44 Å is present only in the Ba-containing samples and is assigned to Ba-Ge correlations. The correlation at 4.66 Å remains a single peak after heating, while two peaks at slightly lower and higher r values are present in Li<sub>2.75</sub>Ge. The origin of the doublet can be attributed to the different second sphere Ge-Ge separations in the "dumbbell" phases (Figure S10a). The fact that the PDF for Li<sub>2,75</sub>Ba<sub>0,19</sub>Ge has a single peak instead of a doublet could suggest the presence of more isolated Ge atoms (i.e., as in Li<sub>7</sub>Ge<sub>2</sub>, Figure S5d) or more disordered orientation between dumbbells. A similar phenomenon was observed in the in situ PDFs obtained during lithiation of Ge nanoparticles, wherein a single broad peak around 4.5-4.6 Å was observed as opposed to the split peak seen in the PDF of dumbbell phases. The broad correlations from 6 to 10 Å in the amorphous sample become sharper and more intense after the heat treatment, suggesting that these interatomic distances become more ordered upon annealing. Refinement of the pattern obtained

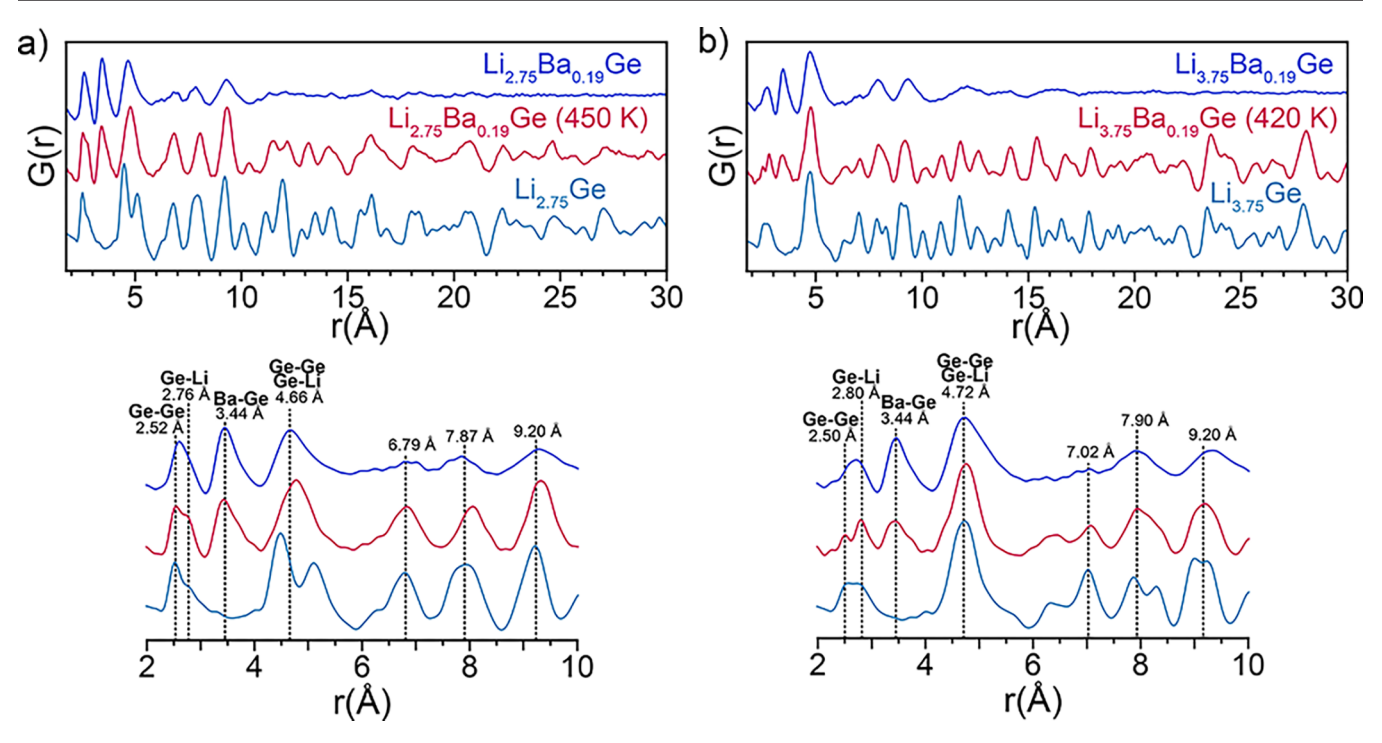


Figure 5. (a) Comparison of PDFs of  $Li_{2.75}Ba_{0.19}Ge$ : unheated (blue), heated to 450 K (pink), and lithiated and unheated α-Ge (light blue). (b) Comparison of PDFs of  $Li_{3.75}Ba_{0.19}Ge$ : unheated (blue), heated to 420 K (pink), and lithiated and unheated α-Ge (light blue). Enlarged regions of 2 < r < 10 Å are shown below. Patterns are y-offset for clarity.

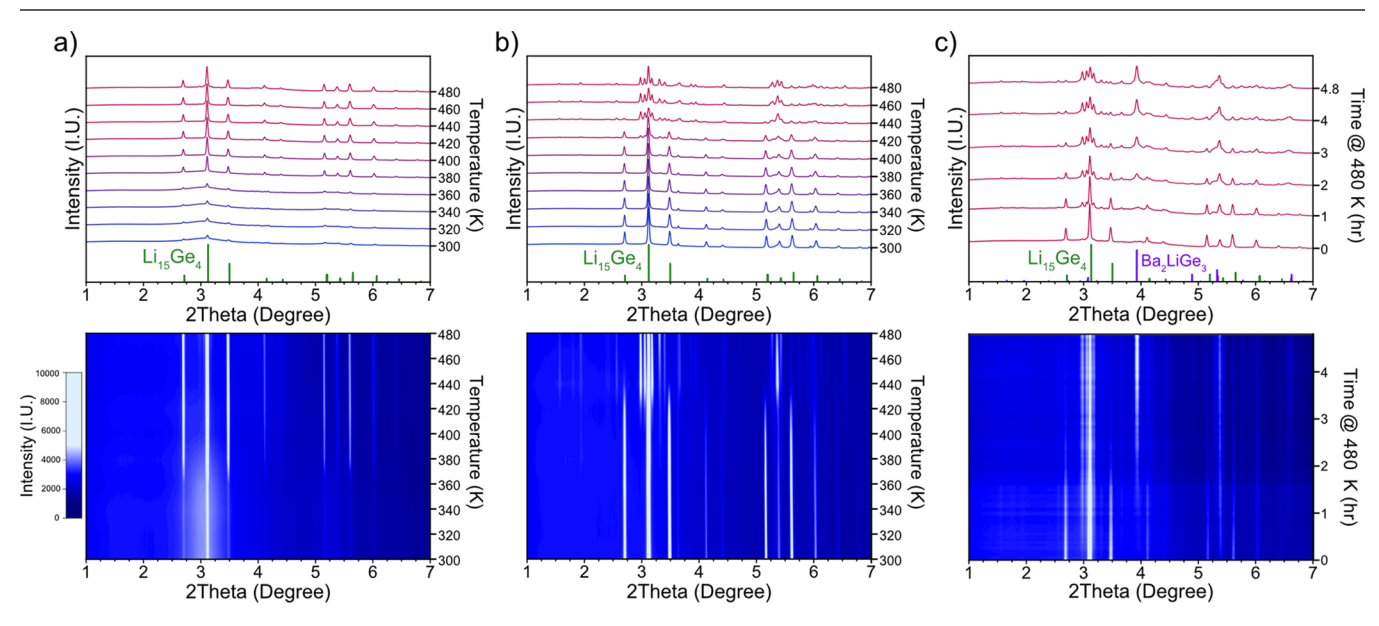


Figure 6. (a, b) Synchrotron XRD results obtained during in situ heating XRD patterns (top) and false colormap (bottom) obtained during heating ramp to 480 K for (a) fully lithiated Ba<sub>8</sub>Ge<sub>43</sub> (Li<sub>3.75</sub>Ba<sub>0.19</sub>Ge) and (b) fully lithiated  $\alpha$ -Ge (Li<sub>3.75</sub>Ge). (c) XRD pattern (top) and false colormap (bottom) of Li<sub>3.75</sub>Ba<sub>0.19</sub>Ge during extended heating at 480 K.

after heating to the structure of  $\text{Li}_7\text{Ge}_2$  resulted in a fit with  $R_w = 55\%$ , which was improved to  $R_w = 28.6\%$  by restricting the fit range to 6–30 Å to exclude the Ba–Ge correlation at 3.44 Å (Figure S11a,b and Table S9). The fairly good fit at higher r values suggests that the long-range order in the  $\text{Li}_{2.75}\text{Ba}_{0.19}\text{Ge}$  phase after heating to 450 K is similar to that found in  $\text{Li}_7\text{Ge}_2$ , implying the presence of dumbbells and isolated Ge atoms. The largest discrepancy in the pattern was at low r values (2–6 Å), suggesting the presence of an amorphous phase probably related to the Ba present in the sample. The correlations

around 6–10 Å are fit well by the  $\text{Li}_7\text{Ge}_2$  refinement, meaning that the broad peaks in the lithiated sample prior to heating are related to the correlations in the crystalline phase formed after heating. In the  $\text{Li}_7\text{Ge}_2$  PDF pattern, the correlations from 6 to 10 Å represent the next nearest neighbor Ge–Ge correlations (either between single atoms or dumbbells), as illustrated in Figure S10b. Since major correlations die out past 10 Å in the unheated  $\text{Li}_{2.75}\text{Ba}_{0.19}\text{Ge}$  sample, it can be presumed that a similar, albeit disordered, structuring of Ge atoms is present in the amorphous sample.

In the PDFs of the fully lithiated samples shown in Figure 5b, the correlations from 2 to 5 Å in the clathrate-derived samples have three main correlations, while there are only two in the  $\text{Li}_{3.75}\text{Ge}$  sample (Figure 5b) due to the absence of Ba—Ge bonding. The broad correlations from 6 to 15 Å in  $\text{Li}_{3.75}\text{Ba}_{0.19}\text{Ge}$  become sharper after heating, an indication of increased ordering, suggesting that the amorphous and crystalline structures are related. On the other hand, *in situ* PDF measurements during heating from 310 to 420 K for the fully lithiated  $\alpha$ -Ge sample (composed predominantly of  $\text{Li}_{15}\text{Ge}_4$ ) were also conducted; however, the pattern showed little change, indicating temperature stability over this range (Figure S12).

Refinement of the PDF from Li<sub>3.75</sub>Ba<sub>0.19</sub>Ge after heating to 420 K showed that the high r features of the PDF could be reasonably captured by the Li<sub>15</sub>Ge<sub>4</sub> phase (Figure S11c and Table S9), suggesting that the long-range order present is from Li<sub>15</sub>Ge<sub>4</sub> correlations. All of the PDFs display a peak around 4.72 Å, which is attributed to the combination of nonbonded Ge-Ge correlations (centered at 4.68 Å) and Li-Ge correlations (shoulder at ~5 Å) found in the crystalline Li<sub>15</sub>Ge<sub>4</sub> phase (see calculated PDF in Figure S10c). The significant discrepancy in the difference curve of the refinement for the heated sample (Figure S11c) suggests the presence of another phase. Due to the decrease in the intensity of the Ba-Ge peak at 3.44 Å after heating, the other phase is likely a Bacontaining amorphous phase. Similar to the Li<sub>2.75</sub>Ba<sub>0.19</sub>Ge sample, the fact that the features from 6 to 10 Å in the PDF of the heated Li<sub>2.75</sub>Ba<sub>0.19</sub>Ge sample can be connected to correlations from the Li<sub>15</sub>Ge<sub>4</sub> crystalline phase suggests that the original features in the unheated sample can be assigned to similar structural features as those found in the crystalline

3.3. Thermal Stability and Crystalline Phase Evolution during Heating. To probe the thermal stability and phase evolution of the amorphous phases formed during electrochemical lithiation of the Ba<sub>8</sub>Ge<sub>43</sub> clathrate, in situ XRD heating experiments were conducted. A heating ramp from 300 to 480 K was performed in 20 K intervals with a 6 min hold at each temperature and scans taken every 2 min. While heating the amorphous Li<sub>3.75</sub>Ba<sub>0.19</sub>Ge sample (Figure 6a), no changes to the pattern were seen until reaching 380 K, at which point reflections corresponding to Li<sub>15</sub>Ge<sub>4</sub> started to appear, consistent with the PDF in situ heating results. There were few additional changes to the XRD pattern with continuous heating up to 480 K. Rietveld refinement analysis showed that the reflections after heating fit well to the Li<sub>15</sub>Ge<sub>4</sub> structure model (Figure S13) and showed a linear increase in a lattice parameter from 10.8119(13) at 360 K to 10.8350(5) at 480 K. In contrast, when performing a similar heat treatment for the  $\text{Li}_{3.75}$ Ge derived from  $\alpha$ -Ge, the XRD pattern transformed from Li<sub>15</sub>Ge<sub>4</sub> into a series of different reflections between 420 and 440 K (Figure 6b).

To further probe the phase transformations in Li $_{3.75}$ Ba $_{0.19}$ Ge, the sample was held at 480 K and XRD scans were collected every 2 min. As shown in Figure 6c, many small reflections and a major reflection at  $2\theta=3.9^{\circ}$  started to appear with further heating as the Li $_{15}$ Ge $_4$  reflections decreased in intensity. Figure 7 compares the XRD patterns for Li $_{3.75}$ Ge and Li $_{3.75}$ Ba $_{0.19}$ Ge after heating at 480 K for 6 and 396 min (6.6 h), respectively, with identification of the reflections from crystalline phases from literature. In the Li $_{3.75}$ Ba $_{0.19}$ Ge sample, the Li $_{15}$ Ge $_4$  transformed to numerous crystalline Li–Ge phases and a

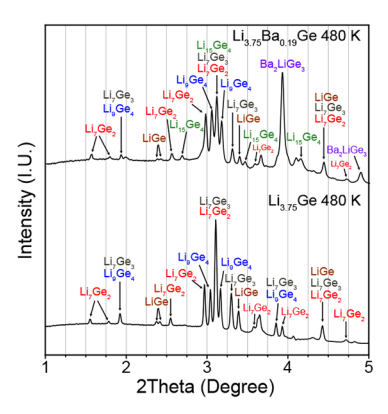


Figure 7. Synchrotron XRD patterns of  $Li_{3.75}Ba_{0.19}Ge$  after heating at 480 K for 6.6 h and  $Li_{3.75}Ge$  after heating ramp to 480 K.

Li-Ba-Ge phase with extended heating at 480 K. The phases identified include LiGe, Li<sub>7</sub>Ge<sub>2</sub>, Li<sub>7</sub>Ge<sub>3</sub>, Li<sub>9</sub>Ge<sub>4</sub>, Li<sub>15</sub>Ge<sub>4</sub>, and Ba2LiGe3. A plot with the reference patterns of the identified compounds is presented in Figure S14. The main reflection for  $Ba_2LiGe_3$  (at  $2\theta = 3.9^\circ$ ) appeared after around 2 h and continued to grow during the 6.6 h hold time, while the reflections from Li<sub>15</sub>Ge<sub>4</sub> transformed completely into the Li-Ge phases after 4 h. In contrast to the Ba-containing sample, the Li<sub>3.75</sub>Ge sample needed less heating to transform to a similar set of Li-Ge phases. From comparison to the reference patterns (Figure S14), the Li<sub>3.75</sub>Ge sample (which showed Li<sub>15</sub>Ge<sub>4</sub> reflections at room temperature) appeared to transform into LiGe, Li<sub>7</sub>Ge<sub>2</sub>, Li<sub>7</sub>Ge<sub>3</sub>, and Li<sub>9</sub>Ge<sub>4</sub> after the 1 h heating ramp from 300 to 480 K. Notably, no reflections from Ba<sub>2</sub>LiGe<sub>3</sub> were present, consistent with the presumed composition of the sample. The similar reaction products observed in both heating experiments suggest that Li<sub>15</sub>Ge<sub>4</sub> decomposition underwent a similar pathway in both Li<sub>3.75</sub>Ba<sub>0.19</sub>Ge and Li<sub>3.75</sub>Ge samples; however, the time needed to achieve the decomposition of Li<sub>15</sub>Ge<sub>4</sub> was longer for the sample derived from lithiation of the Ba<sub>8</sub>Ge<sub>43</sub> clathrate, suggesting a difference in the reaction kinetics.

The thermal decomposition of Li<sub>15</sub>Ge<sub>4</sub> is unexpected as it is a thermodynamically stable phase and melts congruently at 750 °C. <sup>59</sup> Our results show that Li<sub>15</sub>Ge<sub>4</sub> decomposed into Li-Ge dumbbell phases at 150  $^{\circ}$ C, implying that the Li content decreased to the extent that Li<sub>15</sub>Ge<sub>4</sub> was not the preferred phase. Previously, heating studies on electrochemically synthesized Li<sub>15</sub>Si<sub>4</sub>, which is metastable, showed that Li<sub>15</sub>Si<sub>4</sub> decomposed to Li<sub>7</sub>Si<sub>3</sub> and Li<sub>13</sub>Si<sub>4</sub> instead of Li<sub>17</sub>Si<sub>4</sub> and Li<sub>13</sub>Si<sub>4</sub> as expected based on the phase diagram. 46 The authors hypothesized that reactions between Li and the solid electrolyte interphase (SEI) at the electrode/electrolyte interphase or with the electrode binder could reduce the overall Li available in the system to react with Si. This is supported by a study showing that Li<sub>15</sub>Si<sub>4</sub> synthesized via ball milling (i.e., no SEI present) decomposed into the expected products, 60 suggesting that the residual electrolyte and SEI play an important role in the thermal stability of the material. In this work, the in situ heating experiments were conducted in sealed capillaries made of borosilicate, which could also react with Li. However, conducting the same heat treatment using a Ta boat under argon resulted in similar XRD patterns (Figure S15), suggesting that this was not a factor. We conclude that the thermal decomposition of Li<sub>15</sub>Ge<sub>4</sub> at 150 °C is likely related to reactions with the SEI, binder, or residual electrolyte,

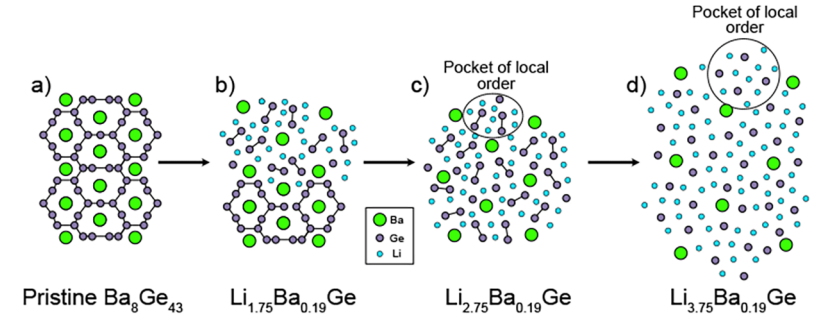


Figure 8. Proposed electrochemical lithiation mechanism of  $Ba_8Ge_{43}$ . (a) In the pristine  $Ba_8Ge_{43}$ , Ba atoms are spread periodically throughout a framework of Ge atoms. (b) Once lithiation proceeds, an amorphous phase nucleates and begins to grow at the expense of the unlithiated crystalline  $Ba_8Ge_{43}$ . (c) After about 2.75 Li per Ge are inserted, complete conversion of the  $Ba_8Ge_{43}$  has occurred, resulting in an amorphous phase composed of pockets with Li–Ge local order between Ba atoms. (d) At full lithiation, the amorphous phase is composed of pockets of Li–Ge with Ge single atoms surrounded by Li.

causing a decrease in the net Li content and leading to the formation of Li–Ge dumbbell phases. Interestingly, the decomposition of Li<sub>15</sub>Ge<sub>4</sub> in the clathrate-derived, Bacontaining phase takes place over a longer period of time than the decomposition of Li<sub>15</sub>Ge<sub>4</sub> derived from lithiation of  $\alpha$ -Ge, implying that the presence of Ba slows these Li–Ge phase transformations.

Considering the final state of the system after the heat treatment, the presence and crystallization of Ba<sub>2</sub>LiGe<sub>3</sub> from the Li<sub>3.75</sub>Ba<sub>0.19</sub>Ge sample indicate that the initial system was far from equilibrium. There are few reported crystalline phases in the Li–Ba–Ge system; thus, when Ba is evenly dispersed between Li and Ge atoms in the amorphous phase, the kinetic barrier to form the set of crystalline phases with the lowest energy is high as this requires a large degree of Ba migration. In addition, the Ba<sub>2</sub>LiGe<sub>3</sub> phase features hexagonal Ge rings (Figure S5f) that would require Ge–Ge bond formation, which is expected to have a higher energy barrier than solely Li rearrangements. <sup>47</sup> Only after 2–3 h of heating at 480 K does Ba and Ge have enough time to coalesce to form Ba<sub>2</sub>LiGe<sub>3</sub>, the presumed Ba-containing equilibrium phase at this composition.

Based on the results from the PDF, XRD, and *in situ* heating experiments, the lithiation of  $Ba_8Ge_{43}$  appears to be heavily influenced by the presence of Ba in the reaction intermediates. In contrast to the crystalline phase transformations for  $\alpha$ -Ge, the clathrate proceeds through lithiation by formation of amorphous intermediates with local structures similar to those in Li–Ge crystalline phases. The PDF heating experiments demonstrate that the amorphous phases that form initially after lithiation have structural relationships to the Li–Ge crystalline phases, evidenced by the ease in which they undergo crystallization at low temperatures. *In situ* XRD heating experiments for the Li<sub>3.75</sub>Ba<sub>0.19</sub>Ge and Li<sub>3.75</sub>Ge samples show that the Li<sub>15</sub>Ge<sub>4</sub> phase, which is formed either electrochemically or by heating the amorphous Ba-containing phase, is unstable at 480 K and decomposes to other Li–Ge phases.

## 4. DISCUSSION

**4.1. Lithiation Mechanism of Ba**<sub>8</sub> $Ge_{43}$ . Overall, the lithiation of Ba<sub>8</sub> $Ge_{43}$  is influenced by the presence of Ba in the reaction intermediates and results in an amorphous lithiation pathway. From the PDF analysis and *in situ* heating experiments, we determine that the amorphous reaction intermediates of Ba<sub>8</sub> $Ge_{43}$  share a local structure like that of the Li–Ge crystalline phases. Therefore, we propose that the

Ba atoms act as "pillars" to prevent the bulk nucleation and growth of Li—Ge crystalline phases during lithiation by physically separating smaller "pockets" of Li—Ge atoms that have a local structure similar to that in the Li—Ge phases.

Figure 8 illustrates the proposed lithiation pathway for the Ba<sub>8</sub>Ge<sub>43</sub> clathrate. Initially, the pristine clathrate has Ba atoms distributed evenly throughout the Ge cage matrix (Figure 8a). As Li enters the system, a two-phase reaction begins with nucleation of an amorphous phase, which is presumed to have similar composition and structure as those seen in the crystalline Li-Ge dumbbell phases. However, the long-range parallel alignment of the Ge-Ge dumbbells (see, e.g., Figure S5a-c) is prevented due to the presence of the Ba atoms. Therefore, the amorphous phase is proposed to consist of Ge-Ge dumbbells surrounded by Li atoms and located in between Ba atoms. This is depicted in Figure 8b, which shows a twophase interface between an amorphous phase (with randomly oriented Ge-Ge dumbbells) and the pristine Ba<sub>8</sub>Ge<sub>43</sub>. As more Li atoms enter the system, the pristine clathrate continues to be consumed and is eventually completely converted to a Li-Ba-Ge amorphous phase. The exact composition is not known, but our results suggest that the conversion is complete by the time the total composition reaches Li<sub>2.75</sub>Ba<sub>0.19</sub>Ge. As seen in the PDF plot of Li<sub>2.75</sub>Ba<sub>0.19</sub>Ge (Figure 3d), the local order extends to  $\sim$ 10 Å, suggesting that the regions of Li-Ge order (indicated by the circled region in Figure 8c) are on this length scale. Considering that the Li<sub>2.75</sub>Ba<sub>0.19</sub>Ge sample crystallized into a structure resembling Li<sub>7</sub>Ge<sub>2</sub> during the *in situ* heating measurement (Figure 4a), we expect that both dumbbells and isolated Ge atoms are present at this point in the lithiation.

With the incorporation of more Li atoms, Ge—Ge dumbbells are broken up in favor of isolated Ge atoms surrounded by Li, as depicted in Figure 8d for the composition Li $_{3.75}$ Ba $_{0.19}$ Ge. At this composition, the local structuring extends further to ~15 Å based on the PDF analysis. This increase suggests the growth of the Li—Ge pocket of local order, which is consistent with the expected volume expansion as more Li atoms enter the system. At this stage, the local structure is similar to that in the Li $_{15}$ Ge $_4$  phase, which is supported by the crystallization of the amorphous phase to Li $_{15}$ Ge $_4$  at 350 K. We note that more detailed modeling of the amorphous phases presented here would require the reverse Monte Carlo method and/or density functional theory calculations and will be reserved for future work.

We conclude that the lithiation pathway for Ba<sub>8</sub>Ge<sub>43</sub> follows an amorphous, metastable phase evolution because of the kinetic differences between the host atoms and the electroactive Li atoms. This is similar to the lithiation of  $\alpha$ -Si, which goes through an amorphous pathway instead of crystallizing to the equilibrium Li-Si phases. 1,2 Because the Si atoms have low mobility at room temperature, phases that rely on Li movement are kinetically favorable. <sup>1,61</sup> Ge has higher mobility at room temperature compared to Si, 62 which accounts for why Li-Ge crystalline phases are kinetically favored to form in some circumstances. In the case of Ba<sub>8</sub>Ge<sub>43</sub>, the mobility of Ba is limited at room temperature, which kinetically traps Ba in the amorphous phase and prevents the formation of a more thermodynamically favorable (i.e., crystalline) phase at these compositions. This conclusion is supported by the in situ XRD heating experiments showing the formation of Ba<sub>2</sub>LiGe<sub>3</sub> after heating at 480 K for multiple hours. On the basis that the Ba<sub>2</sub>LiGe<sub>3</sub> phase is more Ba dense than the Li-Ba-Ge amorphous phase formed after lithiation, a significant amount of Ba migration is needed for Ba2LiGe3 to form. Thus, the presence of Ba between the Li-Ge pockets kinetically frustrates the phase landscape at room temperature, resulting in the formation of amorphous phases.

The fact that Ba<sub>8</sub>Ge<sub>43</sub> undergoes this amorphous lithiation pathway has several effects on its electrochemical profile when compared to that of  $\alpha$ -Ge. Most notably, the voltage of the two-phase reaction for the clathrate is 0.1 V lower than that of the lithiation of  $\alpha$ -Ge (Figure 2). It is well known that amorphous phases will have higher energies than crystalline phases at the same composition. 63-65 Because of the dependence of the chemical potential on the energy of the system,66 the phase with a higher energy will have a lower voltage. Considering that the local environment around Li in the Li-Ba-Ge amorphous phase is similar to that in the Li-Ge crystalline phases, it is expected that the energy will be higher for the amorphous phase, which is consistent with the lower reaction voltage seen for Ba<sub>8</sub>Ge<sub>43</sub>. The presence of Ba in the amorphous phase is expected to further increase the energy of the system due to the donation of electrons from Ba to Ge and thus increasing the electron density on Ge. Ab initio calculations would be needed to understand the contributions of these two separate effects.

In addition to the lower voltage, the lithiation of Ba<sub>8</sub>Ge<sub>43</sub> is characterized by a single voltage plateau in contrast to the two plateaus for  $\alpha$ -Ge. Voltage plateaus originate from the presence of two phases with discrete Li compositions. However, due to the amorphous nature of the intermediates formed upon lithiation of Ba<sub>8</sub>Ge<sub>43</sub>, the crystalline Li-Ge phases typically seen during lithiation of  $\alpha$ -Ge are no longer kinetically accessible, leading to a wider range of possible structures with variable Li content for the clathrate case. After complete conversion of Ba<sub>8</sub>Ge<sub>43</sub> to a Li-Ba-Ge amorphous phase via a two-phase reaction, the Li content in the amorphous phase is allowed to vary continuously as evidenced by the sloped voltage profile, which is indicative of a solid solution mechanism. We liken the lithiation mechanism of Ba<sub>8</sub>Ge<sub>43</sub> to be more similar to that in  $\alpha$ -Si, which first shows a voltage plateau corresponding to a two-phase transformation between the diamond structure and a highly lithiated amorphous phase; after the full conversion of  $\alpha$ -Si, it can be reversibly cycled between amorphous Si and amorphous Li-Si phases.<sup>67</sup> However, in the case of Ba<sub>8</sub>Ge<sub>43</sub>, bulk Li<sub>15</sub>Ge<sub>4</sub> is not formed at the end of lithiation due to the presence of the Ba atoms impeding the long-range order of the Li-Ge pockets.

The voltage profile and corresponding PDF of Li<sub>3.75</sub>Ba<sub>0.19</sub>Ge after delithiation both suggest that the material remains amorphous after the lithium is removed (Figure S7). The voltage profile from delithiation of Li<sub>15</sub>Ge<sub>4</sub> derived from micrometer-sized  $\alpha$ -Ge is characterized by two plateaus attributed to discrete phase transformations between Li<sub>15</sub>Ge<sub>4</sub> and Li<sub>7</sub>Ge<sub>3</sub> at 0.41 V and Li<sub>7</sub>Ge<sub>3</sub> to amorphous Ge at 0.62 V.<sup>41</sup> In contrast, the delithiation of Li<sub>3.75</sub>Ba<sub>0.19</sub>Ge shows a single broad peak at 0.3 V in the dQ/dE plot with a sloped profile, implying solid solution behavior rather than discrete phase transformations. The PDF of the fully delithiated Ba<sub>8</sub>Ge<sub>43</sub> has similar peak positions to the PDF of the pristine clathrate phase (Figure S7d), suggesting that after the removal of Li, a cage-like structure is preserved in this amorphous phase. Future PDF measurements will be needed to further investigate the delithiation mechanism and how the structure evolves with further lithiation cycles.

4.2. Implications for Li-Ion Battery Anodes. Our results indicate several clear differences in fundamental electrochemical and structural properties for the Ba<sub>8</sub>Ge<sub>43</sub> clathrate compared to  $\alpha$ -Ge, which could have advantages in the context of potential use scenarios as anodes in lithium-ion batteries. It is important to note that the crystalline clathrate phase would serve as a precursor to an amorphous phase, which would remain amorphous in subsequent cycles (similar to the lithiation/delithiation of diamond Si). The first potential advantage is that lithiation of Ba<sub>8</sub>Ge<sub>43</sub> proceeds through amorphous solid solutions as opposed to crystalline phase transformations, and bulk crystallization of the thermodynamically stable Li<sub>15</sub>Ge<sub>4</sub> phase is inhibited due to the presence of Ba atoms. Generally, avoiding transformations between crystalline phases can be beneficial for cycling stability by decreasing the tendency for particle damage due to localized stresses, large volume changes, and/or crystallography-related anisotropy in the lithiation strain. <sup>1,9,61,68,69</sup> Future studies will be needed to understand the stress evolution and cycling stability of the amorphous Ba-Ge that forms after the first cycle.

Another benefit of the amorphous lithiation pathway is the decreased reaction voltage of ~0.1 V for lithiation and delithiation of Ba<sub>8</sub>Ge<sub>43</sub> compared to that for  $\alpha$ -Ge. This voltage decrease could lead to increases to the energy density of a full cell. Ba<sub>8</sub>Ge<sub>43</sub> and  $\alpha$ -Ge both react with similar amounts of Li per Ge atom (Figure 2), suggesting that the presence of Ba in the clathrate does not significantly hinder the electrochemical storage. The heavy Ba atoms will lower the gravimetric capacity (1025 mAh/g at Li<sub>3.75</sub>Ba<sub>0.19</sub>Ge) compared to  $\alpha$ -Ge (1386 mAh/g at Li<sub>3.75</sub>Ge); however, we do not expect the volumetric capacity to be significantly different, suggesting that a 0.1 V decrease in reaction potential and a solid solution mechanism could be potentially attractive. In addition, we speculate that the presence of Ba could improve electronic conductivity of the amorphous phase and aid the breaking of Ge-Ge bonds during lithiation due to the excess electrons donated by Ba.

Tetrel clathrates represent a wide design space where the materials can form with different guest atoms, frameworks, and framework substitutions. Herein, we demonstrate how the presence of the Ba atoms prevents the crystallization of Li–Ge phases during electrochemical lithiation. However, there are many more possible compositions of clathrates. For example, type I Ge clathrates have been reported to form with Na, 70

 $K_7^{71,72}$  Sr,  $^{73}$  Rb,  $^{74}$  and  $Cs^{72}$  guest atoms and framework substitutions including Al, 25 Zn, 70 Cd, 72 Ga, 73 and Cu. 75 The large number of compositional and structural possibilities suggests that clathrates could act as precursors to atomically mix elements in a way that results in lithiated amorphous phases with desirable electrochemical properties. For example, substitution of Al for Ge in  $Ba_8Al_\nu Ge_{46-\nu}$  (0 <  $\nu$  < 16) was found to result in a decrease in reaction voltage as the amount of Al increased, with the lowest voltage observed at a composition of Ba<sub>8</sub>Al<sub>16</sub>Ge<sub>30</sub>. Figure S8 shows that Ba<sub>8</sub>Al<sub>16</sub>Ge<sub>30</sub> only required insertion of 1.9 Li to reach full lithiation at 0.06 V versus Li/Li<sup>+</sup> (compared to 3.75 Li for Ba<sub>8</sub>Ge<sub>43</sub>), suggesting possible trade-offs between capacity and voltage for Al substitution. However, PDF analysis showed that Ba<sub>8</sub>Al<sub>16</sub>Ge<sub>30</sub> underwent an amorphization pathway similar to that seen in Ba<sub>8</sub>Ge<sub>43</sub> (Figure S8c), confirming that the voltage profile corresponding to lithiation can be modified (without large changes in the local structure to the resulting amorphous phase) by altering the initial clathrate structure. Future work will need to be conducted to further understand if electrochemical amorphization is unique to the Ba-containing clathrates and which structural conditions result in amorphiza-

## 5. CONCLUSIONS

The lithiation pathway of the type I clathrate Ba<sub>8</sub>Ge<sub>43</sub> was investigated with synchrotron PDF and XRD analyses. Based on the PDF results, Ba<sub>8</sub>Ge<sub>43</sub> proceeds through an amorphous phase transition without formation of any detectable crystalline phases, although future in situ electrochemical studies would be needed to confirm this. Analysis of the PDFs of Ba<sub>8</sub>Ge<sub>43</sub> after lithiation shows that the local order extends to ~10 to 15 Å with similar structural features as those in crystalline Li-Ge phases of analogous composition. This is supported by in situ heating experiments showing that the amorphous Li-Ba-Ge phases crystallized into Li-Ge crystalline phases of similar composition. PDF analysis of Ba<sub>8</sub>Al<sub>16</sub>Ge<sub>30</sub> after lithiation showed that the clathrate transformed to an amorphous phase similar to the one formed upon lithiation of Ba<sub>8</sub>Ge<sub>43</sub>, suggesting that the substitution of Ge with Al on the clathrate framework has little effect on the local structure changes during the reaction.

We propose that the amorphous pathway seen in these clathrates is caused by the presence of the Ba atoms, which act as "pillars" to prevent the crystallization of the Li-Ge domains. The Ba atoms have low mobility at room temperature and are unable to reorder to the more thermodynamically favorable crystalline phases, resulting in a metastable pathway where only significant Li migration is possible. The amorphous reaction mechanism results in a single-phase reaction with a decreased reaction voltage and the suppressed crystallization of Li-Ge phases, which could have beneficial effects on cell performance. Characterization of the clathrate electrodes after lithiation and delithiation shows that despite the crystalline-to-amorphous transition, the local structural features of the original clathrate structure are retained after cycling. Thus, tetrel clathrates have potential use as precursors to atomically mix elements that form an amorphous alloying phase with desirable electrochemical properties. The wide design space for clathrates provides opportunities for optimizing alloying anodes by modification of their initial structure.

#### ASSOCIATED CONTENT

## **Supporting Information**

The Supporting Information is available free of charge at https://pubs.acs.org/doi/10.1021/acs.chemmater.0c03641.

Detailed experimental procedures for the synthesis of type I Ge clathrates, electrochemical measurements, sample preparation for synchrotron measurements, pair distribution function analysis, powder X-ray diffraction, and scanning electron microscopy; supporting tables with the measured voltages and capacity for each sample after electrochemical lithiation; Rietveld refinement parameters for lithiated \alpha-Ge; PDFgui refinement parameters for pristine, lithiated, and heated samples; supporting figures with SEM images of electrodes; plots of PDF refinements for pristine, lithiated, and heated samples; calculated total and partial PDF patterns and crystal structures of reference structures; electrochemical data of  $Ba_8Ge_{43}$  and  $\alpha$ -Ge after one full cycle; electrochemical data and PDFs of Ba<sub>8</sub>Al<sub>16</sub>Ge<sub>30</sub> after lithiation; comparison of total scattering structure function for samples after lithiation and heating; assignment of Ge-Ge correlation distances found in the PDF to distances between Ge atoms in selected dumbbell phases for Li<sub>7</sub>Ge<sub>3</sub>, Li<sub>7</sub>Ge<sub>2</sub>, and Li<sub>15</sub>Ge<sub>4</sub>; Rietveld refinements of XRD patterns for Li<sub>3.75</sub>Ba<sub>0.19</sub>Ge from in situ heating measurements and temperaturedependent lattice parameter for the formed Li<sub>15</sub>Ge<sub>4</sub>; variable-temperature PDF during in situ heating from 310 to 420 K of Li<sub>3.75</sub>Ge; XRD patterns of Li<sub>3.75</sub>Ba<sub>0.19</sub>Ge and Li<sub>3.75</sub>Ge after heating to 480 K and phase identification; and comparison of ex situ laboratory powder XRD pattern of Li<sub>3.75</sub>Ba<sub>0.19</sub>Ge after heating in Ta versus glass capillary (PDF)

# ■ AUTHOR INFORMATION

#### **Corresponding Author**

Candace K. Chan — Materials Science and Engineering, School for Engineering of Matter, Transport and Energy, Arizona State University, Tempe, Arizona 85827, United States; Department of Heterogenous Catalysis, Max-Planck-Institut für Kohlenforschung, 45470 Mülheim an der Ruhr, Germany; orcid.org/0000-0003-4329-4865; Phone: (480) 727-8614; Email: candace.chan@asu.edu

## **Authors**

Andrew Dopilka – Materials Science and Engineering, School for Engineering of Matter, Transport and Energy, Arizona State University, Tempe, Arizona 85827, United States

Amanda Childs – Department of Chemistry and Biochemistry, University of Delaware, Newark, Delaware 19716, United States

Svilen Bobev — Department of Chemistry and Biochemistry, University of Delaware, Newark, Delaware 19716, United States; Ocid.org/0000-0002-0780-4787

Complete contact information is available at: https://pubs.acs.org/10.1021/acs.chemmater.0c03641

#### Notes

The authors declare no competing financial interest.

#### ACKNOWLEDGMENTS

This work was supported by funding from NSF DMR-1710017 and NSF DMR-1709813. A.D. acknowledges support from ASU Fulton Schools of Engineering Dean's Fellowships. C.K.C. acknowledges support from the Max Planck Society and the Alexander von Humboldt Foundation for a Humboldt Research Fellowship. The authors greatly acknowledge the use of facilities within the Eyring Materials Center at Arizona State University supported in part by NNCI-ECCS-1542160. The authors also thank the Diamond Light Source (Didcot, UK) for access to beamline I15-1 (proposal nos. EE21467 and CY22209), T. Forrest and D. Keeble for assistance with PDF measurements, Deutsches Elektronen-Synchrotron (Hamburg, Germany) for access to beamline P02.1 (proposal no. I-20180707), and J. Tseng for assistance with *in situ* heating XRD measurements.

### REFERENCES

- (1) Obrovac, M. N.; Christensen, L. Structural Changes in Silicon Anodes during Lithium Insertion/Extraction. *Electrochem. Solid-State Lett.* **2004**, *7*, A93–A96.
- (2) Limthongkul, P.; Jang, Y. I.; Dudney, N. J.; Chiang, Y. M. Electrochemically-Driven Solid-State Amorphization in Lithium-Silicon Alloys and Implications for Lithium Storage. *Acta Mater.* **2003**, *51*, 1103–1113.
- (3) Yoon, S.; Park, C.-M.; Sohn, H.-J. Electrochemical Characterizations of Germanium and Carbon-Coated Germanium Composite Anode for Lithium-Ion Batteries. *Electrochem. Solid-State Lett.* **2008**, *11*, A42–A45.
- (4) Jung, H.; Allan, P. K.; Hu, Y. Y.; Borkiewicz, O. J.; Wang, X. L.; Han, W. Q.; Du, L. S.; Pickard, C. J.; Chupas, P. J.; Chapman, K. W.; Morris, A. J.; Grey, C. P. Elucidation of the Local and Long-Range Structural Changes That Occur in Germanium Anodes in Lithium-Ion Batteries. *Chem. Mater.* **2015**, *27*, 1031–1041.
- (5) Courtney, I. A.; Tse, J. S.; Mao, O.; Hafner, J.; Dahn, J. R. Ab Initio Calculation of the Lithium-Tin Voltage Profile. *Phys. Rev. B* **1998**, *58*, 15583–15588.
- (6) Graetz, J.; Ahn, C. C.; Yazami, R.; Fultz, B. Highly Reversible Lithium Storage in Nanostructured Silicon Highly Reversible Lithium Storage in Nanostructured Silicon. *Electrochem. Solid-State Lett.* **2003**, *6*, A194–A197.
- (7) Liu, X. H.; Zhong, L.; Huang, S.; Mao, S. X.; Zhu, T.; Huang, J. Y. Size-Dependent Fracture of Silicon Nanoparticles during Lithiation. ACS Nano 2012, 6, 1522–1531.
- (8) Chan, C. K.; Zhang, X. F.; Cui, Y. High Capacity Li Ion Battery Anodes Using Ge Nanowires. *Nano Lett.* **2008**, *8*, 307–309.
- (9) Liang, W.; Yang, H.; Fan, F.; Liu, Y.; Liu, X. H.; Huang, J. Y.; Zhu, T.; Zhang, S. Tough Germanium Nanoparticles under Electrochemical Cycling. *ACS Nano* **2013**, *7*, 3427–3433.
- (10) Su, X.; Wu, Q.; Li, J.; Xiao, X.; Lott, A.; Lu, W.; Sheldon, B. W.; Wu, J. Silicon-Based Nanomaterials for Lithium-Ion Batteries: A Review. *Adv. Energy Mater.* **2014**, *4*, 1300882.
- (11) Wang, J.; Fan, F.; Liu, Y.; Jungjohann, K. L.; Lee, S. W.; Mao, S. X.; Liu, X.; Zhu, T. Structural Evolution and Pulverization of Tin Nanoparticles during Lithiation-Delithiation Cycling. *J. Electrochem. Soc.* **2014**, *161*, F3019–F3024.
- (12) Bourderau, S.; Brousse, T.; Schleich, D. M. Amorphous Silicon as a Possible Anode Material for Li-Ion Batteries. *J. Power Sources* **1999**, *81-82*, 233–236.
- (13) Chevrier, V. L.; Dahn, J. R. First Principles Model of Amorphous Silicon Lithiation. *J. Electrochem. Soc.* **2009**, **2009**156, A454—A458.
- (14) Zhao, L.; Dvorak, D. J.; Obrovac, M. N. Layered Amorphous Silicon as Negative Electrodes in Lithium-Ion Batteries. *J. Power Sources* **2016**, 332, 290–298.
- (15) Liu, X. H.; Huang, S.; Picraux, S. T.; Li, J.; Zhu, T.; Huang, J. Y. Reversible Nanopore Formation in Ge Nanowires during Lithiation-

- Delithiation Cycling: An in Situ Transmission Electron Microscopy Study. *Nano Lett.* **2011**, *11*, 3991–3997.
- (16) Graetz, J.; Ahn, C. C.; Yazami, R.; Fultz, B. Nanocrystalline and Thin Film Germanium Electrodes with High Lithium Capacity and High Rate Capabilities. *J. Electrochem. Soc.* **2004**, *151*, A698–A702.
- (17) Wang, J. W.; He, Y.; Fan, F.; Liu, X. H.; Xia, S.; Liu, Y.; Harris, C. T.; Li, H.; Huang, J. Y.; Mao, S. X.; Zhu, T. Two-Phase Electrochemical Lithiation in Amorphous Silicon. *Nano Lett.* **2013**, 13, 709–715.
- (18) Langer, T.; Dupke, S.; Trill, H.; Passerini, S.; Eckert, H.; Pöttgen, R.; Winter, M. Electrochemical Lithiation of Silicon Clathrate-II. *J. Electrochem. Soc.* **2012**, *159*, 1318–1322.
- (19) Yang, J.; Tse, J. S. Silicon Clathrates as Anode Materials for Lithium Ion Batteries? *J. Mater. Chem. A* **2013**, *1*, 7782.
- (20) Böhme, B.; Minella, C. B.; Thoss, F.; Lindemann, I.; Rosenburg, M.; Pistidda, C.; Møller, K. T.; Jensen, T. R.; Giebeler, L.; Baitinger, M.; Gutfleisch, O.; Ehrenberg, H.; Eckert, J.; Grin, Y.; Schultz, L. B1-Mobilstor: Materials for Sustainable Energy Storage Techniques Lithium Containing Compounds for Hydrogen and Electrochemical Energy Storage. *Adv. Eng. Mater.* **2014**, *16*, 1189–1195.
- (21) Wagner, N. A.; Raghavan, R.; Zhao, R.; Wei, Q.; Peng, X.; Chan, C. K. Electrochemical Cycling of Sodium-Filled Silicon Clathrate. *ChemElectroChem* **2014**, *1*, 347–353.
- (22) Li, Y.; Raghavan, R.; Wagner, N. A.; Davidowski, S. K.; Baggetto, L.; Zhao, R.; Cheng, Q.; Yarger, J. L.; Veith, G. M.; Ellis-Terrell, C.; Miller, M. A.; Chan, K. S.; Chan, C. K. Type I Clathrates as Novel Silicon Anodes: An Electrochemical and Structural Investigation. *Adv. Sci.* 2015, 2, 1500057.
- (23) Peng, X.; Wei, Q.; Li, Y.; Chan, C. K. First-Principles Study of Lithiation of Type I Ba-Doped Silicon Clathrates. *J. Phys. Chem. C* **2015**, *119*, 28247–28257.
- (24) Zhao, R.; Bobev, S.; Krishna, L.; Yang, T.; Weller, J. M.; Jing, H.; Chan, C. K. Anodes for Lithium-Ion Batteries Based on Type I Silicon Clathrate Ba<sub>8</sub>Al<sub>16</sub>Si<sub>30</sub> Role of Processing on Surface Properties and Electrochemical Behavior. *ACS Appl. Mater. Interfaces* **2017**, *9*, 41246–41257.
- (25) Dopilka, A.; Zhao, R.; Weller, J. M.; Bobev, S.; Peng, X.; Chan, C. K. Experimental and Computational Study of the Lithiation of Ba<sub>8</sub>Al<sub>y</sub>Ge<sub>46-y</sub> Based Type I Germanium Clathrates. *ACS Appl. Mater. Interfaces* **2018**, *10*, 37981–37993.
- (26) Dopilka, A.; Peng, X.; Chan, C. K. Ab Initio Investigation of Li and Na Migration in Guest-Free, Type I Clathrates. *J. Phys. Chem. C* **2019**, 123, 22812–22822.
- (27) Tarnev, T.; Wilde, P.; Dopilka, A.; Schuhmann, W.; Chan, C. K.; Ventosa, E. Surface Properties of Battery Materials Elucidated Using Scanning Electrochemical Microscopy: The Case of Type I Silicon Clathrate. *ChemElectroChem* **2020**, *7*, 665–671.
- (28) Scherf, L. M.; Hattendorff, J.; Buchberger, I.; Geier, S.; Gasteiger, H. A.; Fässler, T. F. Electrochemical Synthesis of the Allotrope Allo-Ge and Investigations on Its Use as an Anode Material. *J. Mater. Chem. A* **2017**, *5*, 11179–11187.
- (29) Marzouk, A.; Balbuena, P. B.; El-Mellouhi, F. Open Framework Allotropes of Silicon: Potential Anode Materials for Na and Li-Ion Batteries. *Electrochim. Acta* **2016**, 207, 301–307.
- (30) He, Y.; Lu, X.; Kim, D. Y. A First-Principles Study on Si<sub>24</sub> as an Anode Material for Rechargeable Batteries. *RSC Adv.* **2018**, *8*, 20228–20233.
- (31) Dolyniuk, J.-A.; Owens-baird, B.; Wang, J.; Zaikina, J. V.; Kovnir, K. Clathrate Thermoelectrics. *Mater. Sci. Eng. R* **2016**, *108*, 1–46.
- (32) Rodriguez, S. Y.; Saribaev, L.; Ross, J. H. Zintl Behavior and Vacancy Formation in Type-I Ba-Al-Ge Clathrates. *Phys. Rev. B* **2010**, 82, 1–6.
- (33) Candolfi, C.; Aydemir, U.; Baitinger, M.; Oeschler, N.; Steglich, F.; Grin, Y. Thermoelectric Properties of the Clathrate I  $Ba_8Ge_{43}\square_3$ . *J. Electron. Mater.* **2010**, *39*, 2039–2042.
- (34) Christensen, M.; Johnsen, S.; Iversen, B. B. Thermoelectric Clathrates of Type I. Dalton Trans. 2010, 39, 978–992.

- (35) Takabatake, T.; Suekuni, K.; Nakayama, T.; Kaneshita, E. Phonon-Glass Electron-Crystal Thermoelectric Clathrates: Experiments and Theory. *Rev. Mod. Phys.* **2014**, *86*, 669–716.
- (36) Connétable, D.; Timoshevskii, V.; Masenelli, B.; Beille, J.; Marcus, J.; Barbara, B.; Saitta, A. M.; Rignanese, G. M.; Mélinon, P.; Yamanaka, S.; Blase, X. Superconductivity in Doped Sp<sup>3</sup> Semiconductors: The Case of the Clathrates. *Phys. Rev. Lett.* **2003**, *91*, 247001.
- (37) Hübner, J. M.; Prots, Y.; Schnelle, W.; Bobnar, M.; König, M.; Baitinger, M.; Simon, P.; Carrillo-Cabrera, W.; Ormeci, A.; Svanidze, E.; Grin, Y.; Schwarz, U. In-Cage Interactions in the Clathrate Superconductor Sr<sub>8</sub>Si<sub>46</sub>. *Chem. A Eur. J.* **2020**, *26*, 830–838.
- (38) Bryan, J. D.; Srdanov, V. I.; Stucky, G. D.; Schmidt, D. Superconductivity in Germanium Clathrate Ba<sub>8</sub>Ga<sub>16</sub>Ge<sub>30</sub>. *Phys. Rev. B* **1999**, *60*, 3064–3067.
- (39) Reny, E.; San-Miguel, A.; Guyot, Y.; Masenelli, B.; Mélinon, P.; Saviot, L.; Yamanaka, S.; Champagnon, B.; Cros, C.; Pouchard, M.; Borowski, M.; Dianoux, A. J. Vibrational Modes in Silicon Clathrate Compounds: A Key to Understanding Superconductivity. *Phys. Rev. B* **2002**, *66*, No. 014532.
- (40) Key, B.; Morcrette, M.; Tarascon, J.-M.; Grey, C. P. Pair Distribution Function Analysis and Solid State NMR Studies of Silicon Electrodes for Lithium Ion Batteries: Understanding the (De)Lithiation Mechanisms. J. Am. Chem. Soc. 2011, 133, 503–512.
- (41) Jung, H. Solid State NMR and Pair Distribution Function Analysis Studies of Ge and Sn Anodes for Li-Ion Batteries. Ph.D. Thesis, Stony Brook University, Stony Brook; United States, 2015.
- (42) Lorie Lopez, J. L.; Grandinetti, P. J.; Co, A. C. Phase Transformations and Capacity Fade Mechanism in Li<sub>x</sub>Sn Nanoparticle Electrodes Revealed by Operando <sup>7</sup>Li NMR. *J. Mater. Chem.* A **2019**, 7, 10781–10794.
- (43) Allan, P. K.; Griffin, J. M.; Darwiche, A.; Borkiewicz, O. J.; Wiaderek, K. M.; Chapman, K. W.; Morris, A. J.; Chupas, P. J.; Monconduit, L.; Grey, C. P. Tracking Sodium-Antimonide Phase Transformations in Sodium-Ion Anodes: Insights from Operando Pair Distribution Function Analysis and Solid-State NMR Spectroscopy. *J. Am. Chem. Soc.* **2016**, *138*, 2352–2365.
- (44) Stratford, J. M.; Mayo, M.; Allan, P. K.; Pecher, O.; Borkiewicz, O. J.; Wiaderek, K. M.; Chapman, K. W.; Pickard, C. J.; Morris, A. J.; Grey, C. P. Investigating Sodium Storage Mechanisms in Tin Anodes: A Combined Pair Distribution Function Analysis, Density Functional Theory, and Solid-State NMR Approach. *J. Am. Chem. Soc.* **2017**, *139*, 7273–7286.
- (45) Billinge, S. J. L.; Kanatzidis, M. G. Beyond Crystallography: The Study of Disorder, Nanocrystallinity and Crystallographically Challenged Materials with Pair Distribution Functions. *Chem. Commun.* **2004**, *4*, 749–760.
- (46) Wang, Y.; Dahn, J. Phase Changes in Electrochemically Lithiated Silicon at Elevated Temperature. *J. Electrochem. Soc.* **2006**, *153*, A2314.
- (47) Chevrier, V. L.; Dahn, H. M.; Dahn, J. R. Activation Energies of Crystallization Events in Electrochemically Lithiated Silicon. *J. Electrochem. Soc.* **2011**, *158*, A1207.
- (48) Farrow, C. L.; Billinge, S. J. L. Relationship between the Atomic Pair Distribution Function and Small-Angle Scattering: Implications for Modeling of Nanoparticles. *Acta Crystallogr. Sect. A* **2009**, *65*, 232–239.
- (49) Juhás, P.; Davis, T.; Farrow, C. L.; Billinge, S. J. L. PDFgetX3: A Rapid and Highly Automatable Program for Processing Powder Diffraction Data into Total Scattering Pair Distribution Functions. *J. Appl. Crystallogr.* **2013**, *46*, 560–566.
- (50) Yang, X.; Juhas, P.; Farrow, C. L.; Billinge, S. J. L. xPDFsuite: An End-to-End Software Solution for High Throughput Pair Distribution Function Transformation, Visualization and Analysis. arXiv [cond-mat], 2014, 1402.3163.
- (51) Morris, A. J.; Grey, C. P.; Pickard, C. J. Thermodynamically Stable Lithium Silicides and Germanides from Density Functional Theory Calculations. *Phys. Rev.* **2014**, *90*, 22–24.

- (52) Johnson, Q.; Smith, G. S.; Wood, D. The Crystal Structure of Li<sub>15</sub>Ge<sub>4</sub>. Acta Crystallogr. 1965, 18, 131–132.
- (53) Lim, L. Y.; Liu, N.; Cui, Y.; Toney, M. F. Understanding Phase Transformation in Crystalline Ge Anodes for Li-Ion Batteries. *Chem. Mater.* **2014**, *26*, 3739–3746.
- (54) Tang, W.; Liu, Y.; Peng, C.; Hu, M. Y.; Deng, X.; Lin, M.; Hu, J. Z.; Loh, K. P. Probing Lithium Germanide Phase Evolution and Structural Change in a Germanium-in-Carbon Nanotube Energy Storage System. J. Am. Chem. Soc. 2015, 137, 2600–2607.
- (55) Loaiza, L. C.; Louvain, N.; Fraisse, B.; Boulaoued, A.; Iadecola, A.; Johansson, P.; Stievano, L.; Seznec, V.; Monconduit, L. Electrochemical Lithiation of Ge: New Insights by Operando Spectroscopy and Diffraction. *J. Phys. Chem.* C **2018**, *122*, 3709–3718.
- (56) Hopf, V.; Müller, W.; Schäfer, H. Die Strucktur Der Phase Li<sub>7</sub>Ge<sub>2</sub>. Zeitschrift für Naturforsch. **1972**, 27b, 1157–1160.
- (57) Hopf, V.; Müller, W.; Schäfer, H. Die Kristallstruktur Der Phase Li<sub>o</sub>Ge<sub>4</sub>. Zeitschrift für Naturforsch. 1970, 25b, 653.
- (58) Vaughey, J. T.; Miller, G. J.; Gravelle, S.; Alejandro Leon-Escamilla, E.; Corbett, J. D. Synthesis, Structure, and Properties of BaGe<sub>2</sub>: A Study of Tetrahedral Cluster Packing and Other Three-Connected Nets in Zintl Phases. *J. Solid State Chem.* **1997**, 133, 501–507
- (59) Grüttner, A. Ph.D. Thesis, University of Stuttgart, Stuttgart, Germany, 1982.
- (60) Zeilinger, M.; Baran, V.; Van Wüllen, L.; Häussermann, U.; Fässler, T. F. Stabilizing the Phase  $\mathrm{Li_{15}Si_4}$  through Lithium-Aluminum Substitution in  $\mathrm{Li_{15-x}Al_xSi_4}$  (0.4 < x < 0.8) Single Crystal X-Ray Structure Determination of  $\mathrm{Li_{15}Si_4}$  and  $\mathrm{Li_{14.37}Al_{0.63}Si_4}$ . Chem. Mater. 2013, 25, 4113–4121.
- (61) McDowell, M. T.; Lee, S. W.; Nix, W. D.; Cui, Y. 25th Anniversary Article: Understanding the Lithiation of Silicon and Other Alloying Anodes for Lithium-Ion Batteries. *Adv. Mater.* **2013**, 25, 4966–4985.
- (62) Chou, C. Y.; Hwang, G. S. On the Origin of Anisotropic Lithiation in Crystalline Silicon over Germanium: A First Principles Study. *Appl. Surf. Sci.* **2014**, 323, 78–81.
- (63) Chou, C. Y.; Kim, H.; Hwang, G. S. A Comparative First-Principles Study of the Structure, Energetics, and Properties of Li-M (M = Si, Ge, Sn) Alloys. *J. Phys. Chem. C* **2011**, *115*, 20018–20026.
- (64) Aykol, M.; Dwaraknath, S. S.; Sun, W.; Persson, K. A. Thermodynamic Limit for Synthesis of Metastable Inorganic Materials. *Sci. Adv.* **2018**, *4*, 1–8.
- (65) Sivonxay, E.; Aykol, M.; Persson, K. A. The Lithiation Process and Li Diffusion in Amorphous  $SiO_2$  and Si from First-Principles. *Electrochim. Acta* **2020**, 331, 135344.
- (66) Aydinol, M. K.; Kohan, A. F.; Ceder, G.; Cho, K.; Joannopoulos, J. Ab Initio Study of Lithium Intercalation in Metal Oxides and Metal Dichalcogenides. *Phys. Rev. B* **1997**, *56*, 1354–1365
- (67) Obrovac, M. N.; Krause, L. J. Reversible Cycling of Crystalline Silicon Powder. *J. Electrochem. Soc.* **2007**, *154*, A103.
- (68) Obrovac, M. N.; Chevrier, V. L. Alloy Negative Electrodes for Li-Ion Batteries. *Chem. Rev.* **2014**, *114*, 11444–11502.
- (69) Hatchard, T. D.; Topple, J. M.; Fleischauer, M. D.; Dahn, J. R. Electrochemical Performance of SiAlSn Films Prepared by Combinatorial Sputtering. *Electrochem. Solid-State Lett.* **2003**, *6*, 6–10.
- (70) Stegmaier, S.; Hlukhyy, V.; Fässler, T. F. The Intermetallic Type-I Clathrate  $Na_8Zn_4Ge_{42}$ . Zeitschrift fur Anorg. und Allg. Chemie 2020, 646, 1073–1078.
- (71) Beekman, M.; Nolas, G. S. Transport Properties of the Binary Type I Clathrate  $K_8Ge_{44}\square_2$ . Int. J. Appl. Ceram. Technol. **2007**, 4, 332–338.
- (72) Schäfer, M.; Bobev, S. Synthesis and Structural Characterization of the New Clathrates  $K_8Cd_4Ge_{42}$ ,  $Rb_8Cd_4Ge_{42}$ , and  $Cs_8Cd_4Ge_{42}$ . *Materials* **2016**, *9*, 236.
- (73) Zhang, Y.; Lee, P. L.; Nolas, G. S.; Wilkinson, A. P. Gallium Distribution in the Clathrates  $Sr_8Ga_{16}Ge_{30}$  and  $Sr_4Eu_4Ga_{16}Ge_{30}$  by Resonant Diffraction. *Appl. Phys. Lett.* **2002**, *80*, 2931–2933.

- (74) Schäfer, M. C.; Bobev, S. On the Possibility for Rb- and Eu-Cation Ordering in Type-I Clathrates: Synthesis and Homogeneity Range of the Novel Compounds  $Rb_{8-x}Eu_x(In,Ge)_{46}~(0.6 \le x \le 1.8).$  Acta Crystallogr. Section C 2013, 69, 1457–1461.
- (75) Johnsen, S.; Bentien, A.; Madsen, G. K. H.; Nygren, M.; Iversen, B. B. Copper Containing Germanium Clathrates. *Int. Conf. Thermoelectr. ICT, Proc.* **2005**, 2005, 211–214.